QUANTIFYING PHYSICS AND CHEMISTRY AT MULTIPLE LENGTH-SCALES USING MAGNETIC RESONANCE TECHNIQUES

Lynn F. Gladden*, Michael D. Mantle and Andrew J. Sederman

Department of Chemical Engineering, University of Cambridge, Pembroke Street, Cambridge CB2 3RA, UK

*E-mail: Gladden@cheng.cam.ac.uk

Advances in Chemical Engineering, vol. 30
ISSN 0065 2377
DOI 10.1016/S0065-2377(05)30002-0

Abstract

Magnetic resonance (MR) is finding increasing use in chemical engineering research. The real power of MR techniques is that by bringing together spectroscopy, diffusion, micro-imaging and flow imaging, we have a non-invasive, chemically-specific measurement technique that can characterise a system over length-scales ranging from Å to the cm-scale. The aims of this chapter are two-fold: first, to outline the principles of MR measurements such that they are presented as an integrated set of measurements clearly based on the same physicochemical phenomena; and second, to highlight the recent advances in the field, with a focus on the development of measurement techniques with immediate application to chemical engineering research. The power of bringing together the full range of MR measurements to address phenomena occurring over multiple length-scales is illustrated using examples taken from the field of chemical reaction engineering.

I. Introduction

In recent years there have been notable developments in measurement science and technology, particularly in applications of non-invasive measurement techniques to the chemical and process industries. This interest in implementing modern metrology for the study of multi-component, multi-phase systems is likely to be central to the development of many aspects of chemical engineering research in the coming years. Techniques already established in use include γ- and X-ray absorption, ultrasound attenuation, laser and phase Doppler anemometry, particle-imaging velocimetry and capacitance tomography (Boyer *et al.*, 2002). Of course, there remains significant opportunity to identify new applications of such techniques and to assess and improve the accuracy and spatial and temporal resolution of these measurements, as well as to use these new data to aid in the development and validation of new theoretical or numerical approaches. This chapter focuses on recent developments in magnetic resonance (MR) applications in chemical engineering research, the majority of the examples being drawn from ongoing work in our own research laboratory. MR is a measurement technique that is particularly well suited to providing insight at multiple length-scales. Until recently, each "family" of MR techniques tended to be found in different fields of research. For example, MR spectroscopy (usually referred to as nuclear magnetic resonance, or NMR, spectroscopy) was a tool in common use by chemists and to some extent physicists, while MR imaging (or MRI) was the domain of the medical physicist.

MR diffusion measurements, usually referred to as pulsed field gradient (PFG) or pulsed gradient spin echo (PGSE) techniques, tended to be a niche area of activity undertaken by particular research groups in physics and chemistry laboratories around the world. Clearly, given that these techniques are all based on the phenomenon of the resonant excitation of the nuclear spin system, they can *all* be applied to a given sample within the same sample environment. In many cases, combinations of MR measurements can be integrated into a single MR experiment. For example, why not image (i.e. spatially resolve) a spectroscopic or diffusion measurement? It is when the whole family of MR techniques is brought together that MR has its greatest impact on chemical engineering research, particularly at the level of Å- to cm-scale physical and chemical processes. It is therefore timely that an article is dedicated to the recent developments made in this field and their proven and potential applications.

In addition to the ability of MR to probe a hierarchy of length-scales in a range of systems, the field has been given additional impetus by the development and implementation of "fast" data acquisition techniques. These will be discussed in detail in this chapter. The key development has been to reduce data acquisition times from tens of minutes to tens of milliseconds, making study of the unsteady state possible while retaining all the attributes of chemical specificity, non-invasiveness and transport measurement capability inherent to MR methods. Two major themes are covered in this chapter. First, the recent technical developments in fast data acquisition will be explained and illustrated. Second, an applications focus will be developed: we will look at one case study in particular—that of a fixed-bed catalytic reactor—and review the nature of information that can be obtained over the range of length-scales characterising the system.

Before introducing the principles of MR methods it will be useful to illustrate the multi-scale nature of MR measurements with examples of relevance to chemical engineering that fall outside the scope of the main case study of reaction engineering. The first of these is the field of Rheo–NMR. The current state of the art integrates conventional rheological measurements with MR experimentation. Commercially available sample environments can be purchased such that, for example, a cone-and-plate rheology measurement can be performed *in situ* within the MR magnet, thereby enabling an image of the velocity field within the sample to be acquired during shear. This new type of Rheo–NMR measurement has already produced some important insights. For example, Britton and Callaghan (1997) reported visualisations of anomalous behaviour such as apparent slip, shear banding and fracture during shear measurement in worm-like surfactants (Fig. 1). Quite apart from the interesting rheology under study, this result demonstrates how MR imaging can give us new insights into the limitations of our day-to-day "macroscopic" materials characterisation techniques—in this case, the cone-and-plate rheometer. Obvious questions are: Is the rheometric characterisation provided by the conventional cone-and-plate device giving us all the relevant information about the

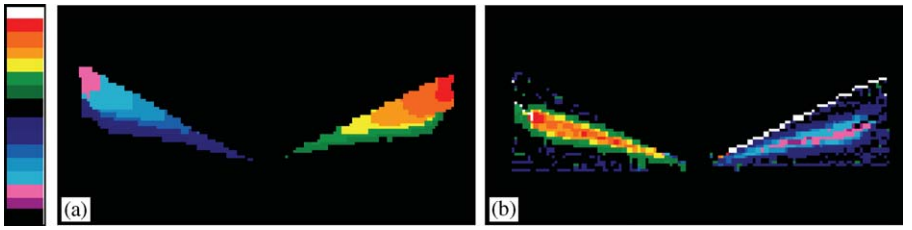

FIG. 1. (a) Velocity image and (b) shear rate map for a worm-like surfactant in a 4° cone gap, at a shear rate of $16\,s^{-1}$ (above critical shear rate). A distinct deviation from a linear velocity gradient and shear banding are observed. The velocity scale lies between the limits ± 12 mm/s and the shear rate between $\pm 57\,s^{-1}$. Reproduced with permission from Britton and Callaghan (1997).

in-use properties of our material? How can we use this new information in optimising product and process performance? *In situ* Rheo–NMR studies can also be combined with *in situ* MR spectroscopy, which then allows us to characterise molecular re-arrangements occurring during shear; such data sets have enormous potential value in testing and validating theoretical models of polymer rheology (e.g. Cormier *et al.*, 2001; Cormier and Callaghan, 2002). At larger length-scales, process applications of Rheo–NMR have been demonstrated with, for example, routine in-line monitoring of shear viscosity–shear rate data (Arola *et al.*, 1997; Powell *et al.*, 1994). The effect of shear on the structural evolution of multi-phase systems during processing operations can also be probed (Altobelli *et al.*, 1997).

A different area of application of MR is that of solids flow. Visualisation of the distribution of solids within vessels by conventional means is limited by opacity; therefore, MR provides one of the few means to visualise structure in particulate arrays and the flow of solids. MR studies of solids are limited to the study of materials that give a detectable MR signal under the relevant experimental conditions—this usually restricts studies to particles that have a liquid-like (i.e. relatively long spin–spin relaxation time—to be discussed later in Section II.B) core. Typical systems are oil-filled plastic beads or seeds which have a naturally high oil content. Early studies focussed on imaging the particle distribution at rest within the container, following perturbations to the system. Such studies have been able to probe convection phenomena within granular systems resulting from vibrations of granular beds (Ehrichs *et al.*, 1995) and to follow the evolution of segregation in rotating granular flow (Hill *et al.*, 1997). Imaging measurements have also been reported while motion is occurring. For example, Seymour *et al.* (2000) have imaged spatial distributions of collisional correlation times during three-dimensional (3-D) granular flow in a horizontal rotating cylinder. A further example has been reported by Metcalfe *et al.* (1999), who reported results of experiments designed to investigate axial transport and core formation in granular systems. Figure 2 shows some images reported from this study—the detail in the internal structure of the bed is clearly seen. MR

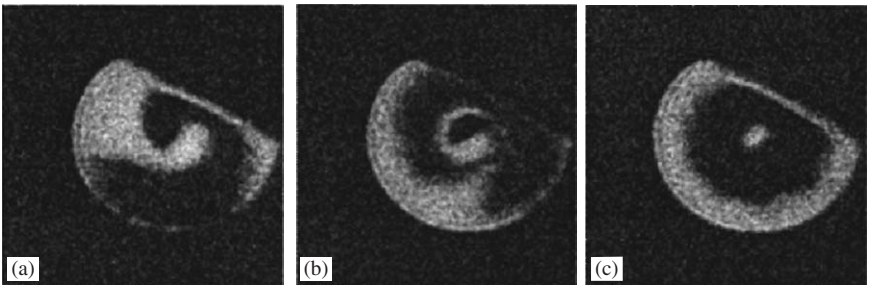

FIG. 2. Central slice of a rotating tube 75% full, with an aspect ratio of 3, comprising mustard seeds (MR active) and polystyrene beads (MR inactive). The mustard seeds are identified as the light grey pixels. The polystyrene beads give no signal intensity. In images (a)–(c) the mustard seeds and polystyrene beads are seen to segregate rapidly but retain a non-mixing core region. Reproduced with permission from Metcalfe *et al.* (1999).

imaging has also been used to visualise formation of bands of high shear within vibrating granular beds (Caprihan *et al.*, 1997), and to quantify the time-averaged density variations and the random motion of granular particles in the presence of gas flow in a model gas-fluidised bed reactor (Savelsberg *et al.*, 2002). Although not performing a spatially resolved (imaging) experiment, Yang *et al.* (2002) have used a pulsed field gradient stimulated echo technique to measure the short time (3-D) displacement, density and granular temperature of mustard seeds vibrated at 15 g in a vertical column of internal diameter 9.0 mm. The behaviour of the dense lower region of the sample was adequately described by inelastic hard-sphere hydrodynamics. However, in the upper layers of the sample, where the mean free path is long, the vertical and horizontal velocities became decoupled, and these observations could not be predicted by current theory.

Hopefully, these examples have given the reader not previously acquainted with MR methods a feel for the potential uses of this field of measurement science in their own research. However, to appreciate the wealth of information that can be obtained from MR measurements, knowledge of the basic principles of MR measurements is required. Therefore, the structure of this chapter is as follows. In Section II, the principles of MR measurements will be described. Sections III and IV report two areas of MR research in which developments of immediate relevance to chemical engineering research have been made. Section III addresses the technical developments made in the field of rapid data acquisition, and examples of data acquired using these new techniques are given. Areas of application are illustrated, examples being chosen from outside the field of reaction engineering to broaden the scope of the chapter. Section IV is dedicated to a case study of reaction engineering studied by MR over a range of length-scales from the Å- and nm-scale behaviour of reactant molecules within the catalyst and the nature of the active site and pore structure of the catalyst, to

the macro-scale hydrodynamics characterising single- and two-phase flow within a fixed-bed reactor packed with catalyst pellets. It is hoped that the reader will see that the same combination of MR methods can be applied to many areas of chemical engineering research including the optimisation of oil recovery processes and the design and control of the manufacture of controlled release pharmaceutical and agrochemical delivery systems, to name just two.

Before proceeding further, it is important that the limitations of MR measurements are identified. In general, we assume that ferromagnetic and paramagnetic systems cannot be studied. However, study of samples and sample environments containing such materials (in small amounts) is sometimes possible. Clearly, from a practical point of view, large ferromagnetic objects cannot be handled within and close to a superconducting magnet. However, sample environments comprising modest amounts of aluminium and brass can be used. With respect to the sample itself, the ability to study a given system is very material-specific. Ferromagnetic and paramagnetic particles, present even at parts per million levels, act to distort the local magnetic fields and relaxation times within the sample, thereby making all studies based upon quantitative analysis extremely difficult. However, depending on the nature of the information that is of interest, systems containing such species can be addressed. MR is also considered to be inherently insensitive compared with other spectroscopic techniques; i.e. it takes 10^{15} nuclear spins to generate a detectable signal. For this reason, gas-phase studies have been a rather specialist area. However, as we will see later (Section III.E), gas-phase studies are now very much a reality with respect to both direct gas-phase imaging and the use of gases as probe molecules to characterise species adsorbed at interfaces.

II. Principles of MR Measurements

There are a large number of different MR techniques that, at first glance, seem quite unrelated. Perhaps the simplest way to look at MR methods is to recognise that they will fall into one of two categories—those that do not require any spatial resolution or positional encoding within the data, and those that do. If you need to encode spatial information in some way, then in addition to a basic MR experiment, which is typically performed in a large, superconducting magnetic field, additional smaller linear gradients in the magnetic field will also be applied at some point during the measurement. This section is set out as follows. In Section II.A, the concepts behind spatially unresolved and spatially resolved experiments are introduced. The simplest MR measurement records a signal proportional to the absolute number of nuclear spins within the system; careful calibration of signal intensity against a reference sample containing a known number of nuclear spins allows the absolute number of spins present in the sample to be quantified which, in turn, yields the number of

species of interest present. Extensions to the MR measurement allow the signal obtained to give quantitative information on the physical–chemical environment of those spins as well as on the temperature and transport processes associated with them—the principles of these measurements are presented in Sections II.B–II.D. In Section II.E, the actual "working" formalism for understanding imaging experiments (known as "pulse sequences") is introduced, and this is then used, in Section II.F, to introduce the principles of "fast" MR measurements. There is no attempt here to give a detailed introduction to the principles of MR techniques; the interested reader should refer to excellent texts by Callaghan (1991) and Kimmich (1997). A very basic introduction to understanding MR spectroscopy measurements and simple imaging sequences (Gladden, 1994) and a more recent, detailed review of fast imaging sequences of relevance to chemical engineering (Mantle and Sederman, 2003) may also be of interest.

A. Spatially Unresolved And Spatially Resolved Experiments

1. Spatially Unresolved Measurements

A spatially unresolved experiment is usually taken to imply a spectroscopy experiment, although relaxation time studies (Section II.B), transport (Section II.C) and temperature (Section II.D) measurements are also often measured as "bulk" properties. The spatially unresolved spectroscopy experiment is the simplest type of MR experiment, and the principles upon which this measurement is based underpins all types of MR measurement, be they spatially unresolved or spatially resolved.

When a nucleus of non-zero nuclear spin quantum number is placed in an external magnetic field (typically a superconducting magnetic field of 2–10 T), its nuclear spin energy levels become non-degenerate. As a result of this, at the equilibrium state of the spin system, there exists a net magnetisation vector aligned parallel to the direction of the external magnetic field, assumed to be along the z-direction. By exposing the system to electromagnetic energy of appropriate frequency (radio-frequency (r.f.)), a resonant absorption occurs between these nuclear spin energy levels. The specific frequency at which this resonance occurs is called the resonance (or Larmor) frequency, and is proportional to the strength of the external magnetic field, B_0, used in the experiment. The precise energy-level splitting is specific to a given isotope of an element, and the resonance frequency (ω_0) is given by

$$\omega_0 = \gamma B_0 \tag{1}$$

where γ is the gyromagnetic ratio, which is an isotope-specific property. The precise energy-level splitting is slightly modified by the electronic environment of the nucleus under study; thus, ω_0 is also modified and becomes specific to

individual molecules containing the element of interest. We can therefore take a spectrum of a mixture of chemical species and identify the presence of particular molecular species in that mixture (i.e. a conventional NMR or MR spectroscopy experiment). In principle (see Section II.B), the measurement is quantitative; i.e. following calibration we know exactly how much of each chemical species is present. A standard way of representing the basic MR measurement is shown in Fig. 3. Initially, the net magnetisation vector, **M**, is aligned along the direction of the magnetic field. The action of the excitation pulse, in this case a pulse of r.f. applied at right angles (along x') to the direction of the superconducting field is to rotate **M** about the x'-axis. In this example, the r.f. excitation is applied for sufficient time so that **M** is rotated to lie along the y'-axis in the x'–y' plane. If this condition is met, the r.f. pulse is referred to as a $\pi/2$ (or 90°) pulse; i.e. it has rotated **M** through $\pi/2$ radians. These processes actually occur in the "rotating frame" of reference (hence the primed symbol) which, in the laboratory frame, precesses about the z-axis (i.e. about $\mathbf{B}_0$) at the Larmor frequency. This con-

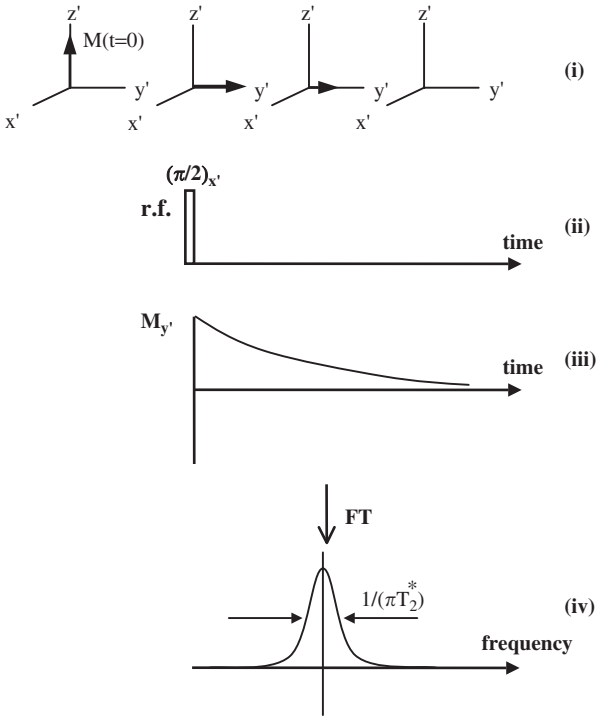

FIG. 3. The behaviour of the magnetisation vector (i) is shown in response to the application of a single $\pi/2$ r.f. pulse along the x'-direction, (ii). The decay of the magnetisation vector in the x'–y' plane yields the received time-domain signal, called the FID, shown in (iii). The result of a digital Fourier transform of the FID is the spectrum shown in (iv). For a liquid-like sample, the full-width at half-maximum-height of the spectral signal is $1/\pi T_2^*$ (see Section II.B).

vention is adopted to simplify the representation of the action of the r.f. pulses. In this rotating frame representation, the MR time-domain signal, following r.f. excitation, is measured by acquiring the signal (i.e. magnitude of the magnetisation vector) aligned along y' as a function of time; this signal will decay with time owing to the recovery of the magnetisation along z' and, at shorter timescales, owing to the loss of phase coherence of the spin isochromats comprising the net magnetisation vector along the y'-axis. These decay processes are termed the spin–lattice and spin–spin relaxation processes and will be discussed further in Section II.B. The decay of the magnetisation along the y'-axis is recorded as a decaying voltage in a receiver coil. Fourier transform of this time-domain signal, usually referred to as the free induction decay (FID) yields the frequency domain spectral response in which the area under the spectral peak, following appropriate calibration, gives a quantitative measure of the number of nuclear spins associated with that spectral frequency (i.e. a quantitative measure of the number of molecules of a given molecular species present). Thus, MR is an intrinsically chemical-specific, quantitative measurement. This is the essential attribute that makes it such a powerful tool in science and engineering research.

2. *Spatially Resolved Measurements*

In the context of this chapter, spatial resolution refers to any MR measurement that requires identification of the spatial location of nuclear spins. As such, spatially resolved measurements include both imaging and transport measurements. To achieve a spatially resolved measurement, the same physical principles and experimental ''excitation-acquire'' strategies required for the spatially unresolved measurements still apply. The basic spatially unresolved experiment is still performed, but by applying a spatially varying magnetic field, in addition to the large static field $\mathbf{B}_0$, the resonance frequency of species within the sample becomes a function of their position along z and the strength of the applied gradient. Thus, for a magnetic field gradient applied along the $z$direction, G_z:

$$\omega_z = \gamma(B_0 + G_z z) \tag{2}$$

Clearly, this is the basis of an imaging experiment; the measurement can be calibrated such that the relationship between resonance frequency and spatial position is known. Figure 4 illustrates the basic principles of an imaging experiment. Without application of the linear gradient in the magnetic field we perform a spatially unresolved experiment; i.e. the water in both test tubes resonates at the same frequency. Therefore, we see only one MR signal, which is a quantitative measure of the total amount of water in the two test tubes. Upon application of the field gradient, the water at every spatial location along the direction of that gradient has a different resonance frequency; therefore, we acquire an FID that represents, after Fourier transformation, a 1-D spatial

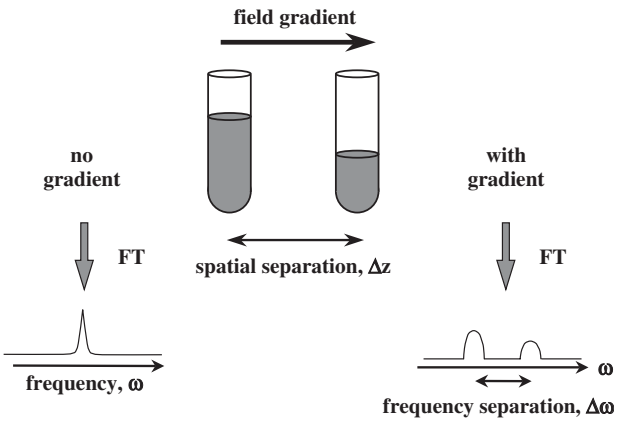

FIG. 4. Consider two test tubes containing different amounts of water. Spatial resolution is obtained by applying a linear gradient in the magnetic field, which makes the resonant frequency of the nucleus of interest a function of its position in real space. Without the presence of the field gradient, the water within the two tubes resonates at the same frequency and a single-peak spectrum is obtained, the area under it being a quantitative measure of the total amount of water in the two tubes. Upon application of the field gradient, the resonant frequency of the water molecules becomes a function of their position along the direction of the applied field gradient. Fourier transform of the acquired signal yields a 1-D profile of the amount of water present. The area under each "peak" gives the amount of water in each tube.

projection (along the direction of the applied gradient) of the amount of water in the two tubes. 2-D and 3-D images are acquired by applying gradients in 2 and 3 orthogonal directions, respectively. However, just as importantly, we see from Eq. (2) that if the application of a magnetic field gradient encodes a given nucleus by its spatial position, then by developing a pulse sequence which allows us to measure the change in position in a given time interval, we have the basis of a MR measurement of transport. This is indeed the principle of the majority of MR transport measurement techniques, e.g. PGSE, often called PFG, measurements of molecular diffusion and MR flow-imaging measurements. The detailed principles of transport measurements are described in Section II.C.

In addition to measurements of "how much" and "what type" of chemical species is present, modification of the MR experiment allows us to quantify the physical state of that species (e.g. gas, liquid, gel, solid), temperature and, as has just been alluded to, any incoherent or coherent transport processes within the system of interest. By integrating any of these measurements into an imaging experiment, we can spatially map these quantities or exploit the effect of these characteristics on the magnitude or frequency of the MR signal to preferentially observe sub-populations of spins within the system. In this latter application we are exploiting so-called "contrast" mechanisms in the image acquisition. These concepts will be illustrated in Sections II.B–II.D.

B. Nuclear Spin Relaxation Times

In the following section, the principles of nuclear spin relaxation processes will be summarised and their use in data acquisition discussed. Following the application of the r.f. excitation pulse, the nuclear spin system has excess energy. To return to equilibrium the spin system has to recover its initial energy and entropy states a process known as ''relaxation''. A number of different relaxation times characterise the mechanisms for the processes involved. The most important are the spin–lattice relaxation (T_1) and spin–spin relaxation (T_2) time constants. These time constants characterise the physicochemical environment of the molecules being studied. T_1, as the name suggests, characterises the energy exchange between the excited spin and the surrounding physical environment (i.e. the lattice), while T_2 characterises the loss of phase coherence between nuclear spins within the nuclear spin ensemble. If a system is characterised by a very small T_2 (e.g. many solids) it may not be possible to study it using MR; this is the major limitation in imaging the solid state. Each chemical species will have its own T_1/T_2 characteristics, and these will vary depending on the physical state in which that species exists.

1. Spin–Lattice Relaxation, T_1

As shown in Fig. 5, before application of the r.f. excitation pulse the net magnetisation vector associated with the nuclear spin system is aligned along the direction of the static magnetic field. It is the magnitude of this vector that provides the quantitative measurement of the number of nuclear spins excited within the sample. After excitation by a $\pi/2$ r.f. pulse applied along the x'-axis, the magnetisation vector is rotated through $\pi/2$ to lie along the y'-axis. As soon as the excitation stops, the system acts to return to equilibrium; this corresponds to a monotonic increase in the magnitude of the magnetisation vector back along z' ($\equiv z$) as a function of time. If we wait a short time, only a fraction of the magnetisation will have been re-established along z'. If we wait ~5–7 T_1, the full magnitude of the magnetisation will have recovered along z'. The magnitude of the magnetisation vector along z', $M_{z'}$, as a function of the ''waiting'' time, τ, can be written down analytically for any specific r.f. pulse sequence. Equation (3) describes the recovery of the magnetisation back along z for a saturation recovery pulse sequence:

$$M_{z'}(\tau) = M_0[1 - \exp(-\tau/T_1)] \tag{3}$$

By recording $M_{z'}$ for a number of τ values and fitting these data to Eq. (3), both the T_1 characterising the system and the value of M_0 (which quantifies the number of initially excited spins) are obtained. In a spatially resolved ''relaxometry'' experiment, images are acquired at different values of τ, and a fit of Eq. (3) to the intensity as a function of τ, for the equivalent pixel, i, in each image allows a complete map of M_{0i} and T_{1i} to be obtained. Thus, spatial variation in

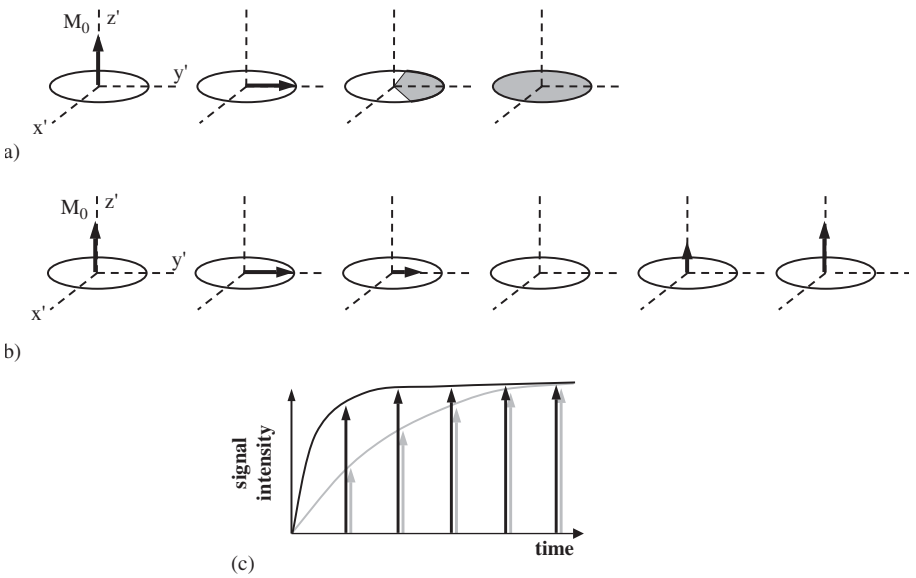

FIG. 5. (a) As described in Fig. 3, the action of the $\pi/2$ pulse (applied along the x' direction) is to rotate the magnetisation vector into the x'–y' plane, along the y'-direction. The individual spin isochromats then dephase in the x'–y' plane, as shown by the increasing size of the shaded region with time. (b) At timescales longer than T_2, the magnetisation recovers back along the direction of the magnetic field B_0, with a characteristic time constant T_1. (c) Two different species within the same sample may have different characteristic T_1 values. In this example, the species associated with the black arrows has a shorter T_1 than the species associated with the grey arrows; the arrows indicate the magnitude of the acquired signal intensity following the initial r.f. excitation. If data are acquired at long times after r.f. excitation, equal signal intensity will be acquired from both species. However, if data are acquired very soon after the excitation pulse, the acquired signal will be predominantly associated with the species characterised by the shorter T_1. This illustrates the principle of relaxation contrast.

T_1 can be mapped throughout the image. Figure 5 also demonstrates that the magnitude of the signal we will acquire will depend on the time at which we acquire the signal. Thus, if we have two species with different T_1 characteristics, by careful selection of the delay time between excitation and acquisition of the resulting signal, a signal can be acquired preferentially from one of the components.

2. *Spin–Spin Relaxation, T_2*

On timescales of less than or equal to that of T_1, spin–spin relaxation (T_2) processes occur. T_2 characterises the loss of phase coherence of the individual spin isochromats within the spin ensemble comprising the total magnetisation vector M_0. A spin isochromat represents a group of spins that experiences the same homogeneous magnetic field and which, therefore, behaves in the same

way following the excitation pulse. During the period following excitation, the individual isochromats will lose phase coherence with each other as a result of spin–spin interactions and local variations in B_0. The decay of the coherent magnetisation aligned along y', due to spin–spin interactions but not magnetic field heterogeneities, is characterised by the time constant T_2 and measured using a "spin-echo" pulse sequence, as shown in Fig. 6. T_2 is defined as follows:

$$M_{y'}(\tau) = M_0 \ \exp(-\tau/T_2) \tag{4}$$

With reference to Fig. 6, $\tau = 2t_{\mathrm{d}}$ in Eq. (4). The π pulse acts to reverse the dephasing effects due to the local heterogeneities in B_0 such that the final acquired signal (the "echo") suffers attenuation due to spin–spin interactions only. The spin-echo shown in Fig. 6, or rather "echoes" in general (since they can be produced by actions other than a π pulse) have widespread use in MR methods, far beyond simple measurement of T_2. In short, by using an echo sequence, instead of exciting the system and then allowing the magnetisation to decay to zero as in Fig. 3, the majority of the magnetisation can be recovered for use in subsequent measurements. The simple "echo" sequence shown in Fig. 6 is a common feature of MR imaging pulse sequences (e.g. Fig. 12).

An additional and important relaxation time constant is T_2^*, which characterises a faster decay of the magnetisation along y' and accounts for, in particular, the additional effects of magnetic field heterogeneities on the loss of phase coherence of the magnetisation. Thus, the simple pulse-acquire sequence (with no re-focusing) shown in Fig. 3, will give a response in which the envelope

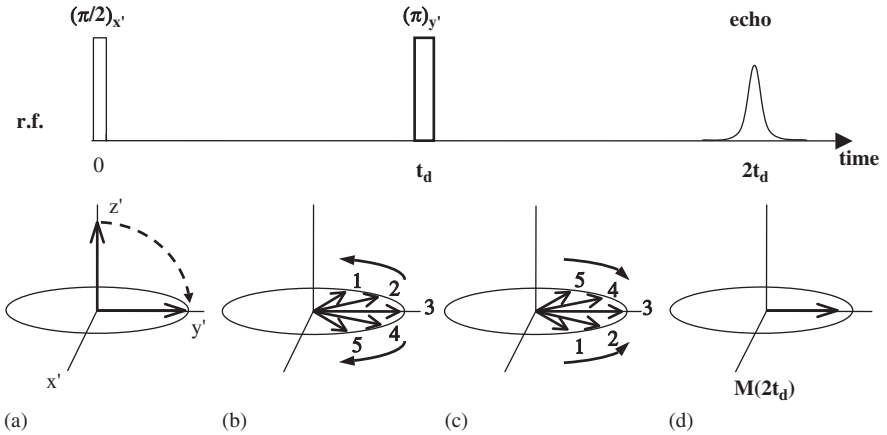

FIG. 6. A spin-echo pulse sequence used to determine T_2. (a) A $(\pi/2)_{x'}$ pulse puts M_0 into the y'-direction, and (b) the spin isochromats dephase with time. At a time t_d later, a π pulse is applied along the y'-axis causing the spins to rotate through π radians (c) such that they "refocus" along the y'-axis to form an "echo" at time. $2t_{\mathrm{d}}$.(d) The decrease in magnitude of the magnetisation vector between stages (a) and (d) provides a measure of T_2 [Eq. (4)]. All "reversible" contributions to the spin-spin relaxation process are removed by the application of the π pulse.

of the decay in the time domain and hence the width of the frequency-domain signal is characterised by T_2^*.

In summary, the reasons that the nuclear spin relaxation times, and in particular T_1 and T_2, are so important are:

(i) Each molecule in a given physicochemical environment is characterised by specific values of T_1 and T_2. Hence, by knowing the T_1 and T_2 characteristics of the species in each state of matter or for each chemical species in a mixture we are able to obtain a wealth of information about a multi-component, multi-phase system.

(ii) The timings of the MR experiment (pulse sequence) allow us to control the extent to which we acquire a signal from the entire spin population. To acquire spectra or image data that are fully quantitative in terms of the signal intensity yielding a true measure of the number of species of interest present, the relaxation times of that system must be measured and the pulse sequences optimised such that any reduction in signal intensity leading to loss of quantitation is avoided. If, as in some cases, it is impossible to implement a pulse sequence without the effects of relaxation "contrast" on the signal intensity, it is possible (but often non-trivial) to correct the signal intensities to their true values as long as the accurate values of the appropriate relaxation times are known.

(iii) In a multi-component or multi-phase system, each component/phase will be characterised by different relaxation times. Therefore, the timings in the MR pulse sequence can be set so that the signal is preferentially acquired from one component/phase. This approach has been exploited in, for example, studies of the separation of an oil–water emulsion in which the T_1 characteristics of the oil and water phases are significantly different (Kauten *et al.*, 1991). Relaxation contrast can also be used to discriminate between liquid and solid phase of the same material during a crystallisation process (e.g. Simoneau *et al.*, 1991).

C. Transport

Transport processes are measured by means of applying pulsed magnetic field gradients to the system, in addition to the normal r.f. pulses. PFG techniques measure molecular displacement as a function of time without the need for introducing tracers into the experiment. The principle of the experiments is easy to understand although the detailed implementation of the experiments is somewhat more challenging. The application of a pulsed field gradient at the beginning of an experiment (i.e. immediately after r.f. excitation) encodes a given spin with a "label" describing its position along the direction of that applied field gradient. At a time Δ later, referred to as the observation time, a second pulsed field gradient is applied. The net effect of applying these two

gradients separated by time Δ is that we can monitor the distance travelled during a known time and hence quantify the transport process of interest.

Figure 7 shows the principles of transport measurement. When considering the application of pulsed magnetic field gradients to measure transport processes we use the lower-case symbol **g**, as opposed to **G**, which is reserved for use in describing the *imaging* gradients [see Eq. (2) and Section II.E]. Perhaps the most important point to appreciate with respect to MR measurements of transport is that the same measurement methodology is used to quantify incoherent (e.g. diffusion, dispersion) and coherent (e.g. flow) processes occurring within the same system. The basic principle derives directly from Eq. (2). If the magnetic field gradient is applied for a short time period (ie. a ''pulse''), as opposed to ''continuously'' during which time data are acquired, instead of imposing a time-independent modified resonance frequency on a nucleus as determined by its spatial position, the nuclear spin is given *phase offset* (say ϕ_1)

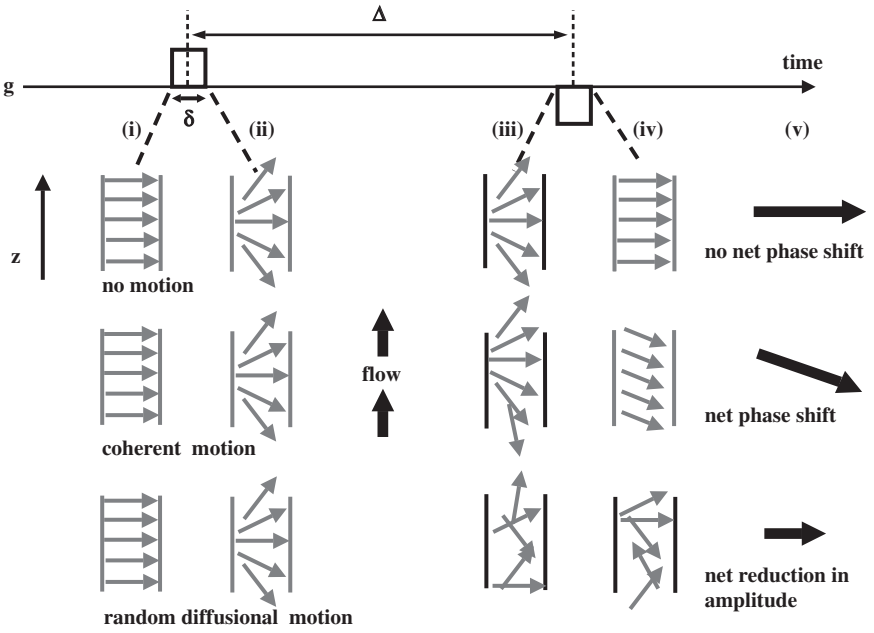

FIG. 7. The principle of transport measurements using the ''phase shift'' approach. Two pulsed magnetic field gradients (of magnitude g and duration δ) are applied a time Δ apart. The cases of no motion, coherent motion (i.e. constant velocity) and random diffusional motion are shown. The schematics show the relative phase offsets of the spin isochromats initially at different positions in z along the length of the sample. (i) Initially all the spins are aligned in the rotating frame. (ii) The first gradient pulse applies a phase offset to the spin isochromats depending on their position along the z-direction. (iii) The position of the spin isochromats after the systems has evolved for the time Δ. (iv) The orientation of the spin isochromats after the action of the second, equal and opposite polarity gradient pulse. (v) The magnitude and phase shift of the net magnetisation vector after application of this bipolar gradient pair (i.e. equal and opposite) pulse sequence.

after application of the pulse characteristic of its spatial position when the pulse was applied. In the rotating frame of the spin system, this phase offset, ϕ_1, is equal to $\gamma g \delta z_1$, where δ is the duration of the applied gradient, z_1 the position of the spin and g the magnitude of the magnetic field gradient along the z-direction. Although many variations on the theme exist, the basic concept underpinning the vast majority of transport measurements is that after an observation time, Δ, an equal but opposite polarity magnetic field gradient pulse is applied, which gives the spins a further phase offset, ϕ_2, such that the total phase offset is $\phi_1 + \phi_2 = \gamma g \delta (z_1 - z_2)$. Clearly, if the molecule (i.e. spin) has not moved during the time Δ, it will experience a net phase shift of $\phi_1 + \phi_2 = 0$; i.e. the magnetisation vector will again be aligned along the y'-axis, as it was immediately after application of the initial excitation pulse. However, if the molecule has moved during the time Δ, i.e. $z_1 \neq z_2$, then $\phi_1 + \phi_2 \neq 0$, and observation of the magnetisation will show a phase shift that is proportional to the distance moved $(z_1 - z_2)$. Since γ, g and δ are known, the displacement or average velocity over the timescale Δ is obtained. A typical transport measurement would proceed by making several measurements at differing values of δ or g and recording the resulting phase shift and amplitude of the signal.

Let us now consider, in detail, the effect on the acquired signal of a *coherent* transport process (i.e. the molecules move with a velocity v in the direction of the applied pulsed gradients). With reference to Fig. 7, we see that the effect of the second pulsed gradient is to re-align the spin isochromats with each other, but at an increasing angle (phase offset) with respect to the y'-axis. As δ or g increases, the net magnetisation will rotate through the x'–y' plane of the rotating frame. This manifests itself as a continuously increasing phase shift, while the magnitude of the magnetisation vector (i.e. signal amplitude) remains constant (ignoring relaxation effects). If only the real component of the complex signal is recorded (i.e. we observe the magnitude of the magnetisation vector projected along y'), an oscillatory signal is recorded as a function of δg, and the period of the oscillation is directly related to the velocity of the moving spins. In the case of an *incoherent* transport process, the random molecular displacements cause a random distribution of phase shifts of the individual spins and the acquired signal is a vector sum of these phase shifts. As δ or g increases, the magnitude of the acquired signal decreases monotonically. An interesting extension to this is when the diffusion occurs within a confined geometry (e.g. an emulsion droplet). In this case, the distance travelled is constrained to a maximum value. Therefore, by taking measurements at increasing values of Δ, a value of Δ is reached, above which no further signal attenuation is measured—this value of Δ quantifies the typical dimension of the discrete phase. When pulsed magnetic field gradients are applied to study diffusive processes, the MR technique is often referred to as PFG or PGSE-MR. Application of PGSE-MR techniques to quantify molecular diffusion was pioneered by Stejskal and Tanner (Stejskal, 1965; Stejskal and Tanner, 1965), and the techniques typically probe molecular displacements of 10^{-6}–10^{-5} m over timescales of order

10^{-3}–1 s. An overview of applications of PGSE-MR in chemical engineering is given elsewhere (Gladden, 1994).

Transport measurements performed using pulsed magnetic field gradients are more clearly understood using a more mathematical framework. It follows from Eq. (2) that the phase shift (i.e. the instantaneous phase offset in resonance frequency) $\phi(t)$ acquired in the rotating frame following application of a magnetic field gradient, g, along the z-direction, will be

$$\phi(t) = \gamma \int_0^t \mathrm{g}(t) z(t)\, \mathrm{d}t \tag{5}$$

We also know that the change of position with time of a "spin" or its associated magnetic moment can be written as

$$z(t) = z_0 + vt + \tfrac{1}{2}at^2 + \cdots \tag{6}$$

where z_0 is initial position, v the velocity and a the acceleration in the direction of the gradient. Substituting Eq. (6) into Eq. (2) gives:

$$\omega(t) = \gamma\left[B_0 + \mathrm{g}\left(z_0 + vt + \tfrac{1}{2}at^2 + \cdots\right)\right] \tag{7}$$

The total relative phase of the MR signal is then calculated by considering the time integrals of the individual terms on the right-hand side of Eq. (7). These integrals are the *moments* of the magnetic field gradient and the zeroth, first, and second are proportional to

$$\text{zeroth moment}: \quad z_0 \int \mathrm{g}(t)\, \mathrm{d}t \tag{8}$$

$$\text{first moment}: \quad v \int \mathrm{g}(t) t\, \mathrm{d}t \tag{9}$$

$$\text{second moment}: \quad \frac{1}{2} a \int \mathrm{g}(t) t^2\, \mathrm{d}t \tag{10}$$

Let us now consider the action of the two equal and opposite pulse gradients (referred to as a bipolar pair) shown in Fig. 7 of amplitude $\pm$g and length δ, separated by time Δ. The first pulse, $+$g, will, in the absence of relaxation, cause a phase shift according to the integral defined by the zeroth moment:

$$\int_0^{\delta} \mathrm{g}(t)\, \mathrm{d}t = [\mathrm{g}t]_0^{\delta} = \mathrm{g}\delta \tag{11}$$

The second, equal and opposite, gradient pulse will have a zeroth moment given by

$$\int_{\Delta}^{\delta+\Delta} g(t)\,dt = [-gt]_{\Delta}^{\delta+\Delta} = (-g\delta - g\Delta) - (-g\Delta) = -g\delta \tag{12}$$

Addition of Eqs. (11) and (12) gives the total relative phase shift which, for the case of no motion, is clearly zero.

Now consider the evaluation of the first moment when the magnetic moment undergoes motion at a constant velocity v in the direction of the gradient. The total first moment is given by

$$\int_{0}^{\delta} g(t)t\,dt + \int_{\Delta}^{\Delta+\delta} g(t)t\,dt = \frac{1}{2}g\left(\delta^2 - 0 - \Delta^2 - 2\delta\Delta - \delta^2 + \Delta^2\right) = -g\delta\Delta \tag{13}$$

Therefore, the residual phase shift of the MR signal for a magnetic moment undergoing uniform motion with velocity v for a set of bipolar gradients, $\pm g$, of duration δ separated by time Δ is $-\gamma v g\delta\Delta$, i.e. the measured phase shift is linearly proportional to the velocity.

In practice, we may wish to measure only one of the moments (Eqs. (8)–(10)), thereby removing the sensitivity of the measurement to position, velocity or acceleration. This is done by modifying the basic transport measurement pulse sequence (Fig. 7) so that the integrals are zero for all moments except the one that is to be measured. These so-called "compensated" pulse sequences have been reviewed in detail by Pope and Yao (1993a). Figure 8 shows the effect of gradient nulling on a system of mustard seeds in a rotating drum (Fukushima, 1999). Figure 8a is taken with a sequence in which only the zeroth moment of

(a) (b) (c)

FIG. 8. Mustard seeds flowing in a drum. (a) Only the zeroth moment is nulled, and the image shows significant signal attenuation (visible as the lighter shades in the sliding layer) due to the velocity distribution in each pixel and higher-order contributions. (b) The first moment is nulled. There is no signal loss due to the velocity distribution; the remaining signal attenuation reflects velocity fluctuation and diffusion in the presence of background gradients. (c) Diffusion image. The darkness of the image is proportional to the diffusion coefficient D perpendicular to the plane of the image, calculated from signal attenuation in the presence of a gradient applied along the cylinder axis. All images were acquired at a ^{1}H frequency of 80 MHz. Reprinted with permission from Fukushima (1999), copyright 1999, Annual Reviews www.annualreviews.org.

the magnetic field gradients is zero. The signal loss along the exposed edge, visible as lighter shades in the image, is due to the velocity distribution as well as higher order motions. Figure 8b was recorded with an imaging sequence in which the first moment was made zero. The signal is much stronger because there is no signal loss due to the velocity distribution. Figure 8c shows an image that has been encoded for diffusive motion along the cylinder axis; darker regions correspond to a higher diffusion coefficient.

Another type of experiment commonly used when wishing to characterise transport phenomena is the propagator measurement. The propagator gives a statistical description of the evolution of motion characterising the system; it provides a complete description of the random (e.g. diffusion) as well as coherent motions. The propagator, $P_s(\mathbf{r}|\mathbf{r}',t)$, gives the probability of finding a spin initially at $\mathbf{r}$ at time $t = 0$, and at $\mathbf{r}'$ after a time t. If the propagator only depends on the displacement $\mathbf{R} = \mathbf{r}' - \mathbf{r}$, we can define the average propagator:

$$\bar{P}_s(\mathbf{R}, t) = \int P_s(\mathbf{r}|\mathbf{r} + \mathbf{R}, t)\rho(\mathbf{r})\, d\mathbf{r} \tag{14}$$

where $\rho(\mathbf{r})$ is the spin density (i.e. number density of MR active nuclei) at position $\mathbf{r}$. Let us consider the same pair of gradients as shown in Fig. 7. In the case that a molecule moves from z_0 to z' during the time Δ, the net phase shift, Φ, following the second gradient pulse is determined by the zeroth moment, provided that the displacement of the molecule is small during the time the pulse is applied (δ):

$$\Phi = \gamma\delta g(z_0 - z') \tag{15}$$

Defining a dynamic displacement $Z = z' - z_0$, and the average displacement propagator $\overline{P_s}(Z, \Delta)$ as the average probability that any molecule in the sample will move by a displacement Z over time Δ, the acquired signal (relative to that acquired when no magnetic field gradients are used) for a population of spins characterised by a range of displacements is given by

$$\int \overline{P_s}(Z, \Delta)\ \exp(i2\pi qZ)\, dZ \tag{16}$$

where $\mathbf{q} = (1/2\pi)\gamma\delta\mathbf{g}$ is the reciprocal displacement vector (Callaghan, 1991). The average displacement propagator distribution, $\overline{P_s}(Z, \Delta)$, is obtained by Fourier inversion of the acquired MR signal. The propagator measurement is equivalent to a tracer measurement in which the tracer is introduced into the flow and the average distribution of tracer from its location determined in a completely non-invasive manner. Figure 9 shows propagators determined for water flow within a packed bed of spheres. The major features of propagator measurement are clearly seen. As the observation time increases, the peak in the propagator occurs at a greater displacement, and the width of the propagator

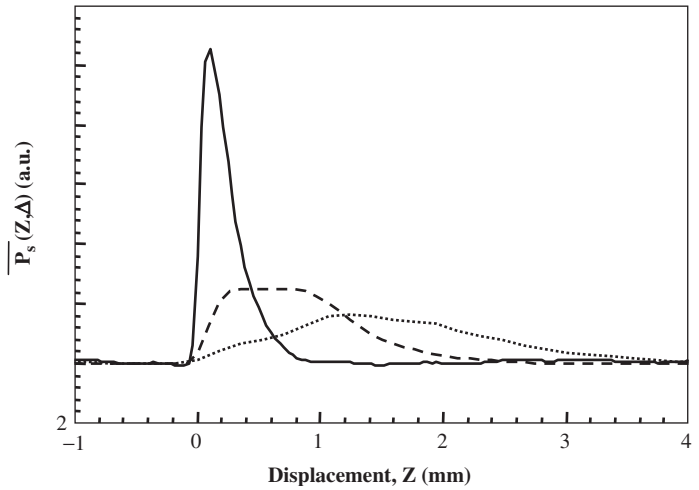

FIG. 9. Displacement propagators recorded for flow of water through a packed bed of 1 mm diameter glass beads packed within a 10 mm diameter column. The average flow velocity was 0.77 mm/s, corresponding to *Pe* and *Re* of 350 and 0.77, respectively. Propagators are shown for observation times, $\Delta = 0.3$ s (—), 1 s (- - - -) and 2 s (· · · · ·).

distribution increases, reflecting the magnitude of molecular diffusion and dispersion phenomena occurring within the bed.

For obvious reasons, the methods just described are termed "phase shift" measurements of transport. These methods are considered the most robust and quantitative, and are therefore the most commonly used. Another approach is time-of-flight (TOF) imaging. TOF or "spin tagging" methods were first reported by Singer (1959), and their use has been widespread since then, particularly with respect to velocity measurement, although the same measurement also probes other transport processes. At its simplest, the TOF approach monitors velocity by the attenuation observed in the acquired image—no absolute, direct measure of velocity using pulsed gradients is employed. The principle is that a set of spins are given an initial excitation pulse—signal will only be acquired from these excited spins at a given time later. Thus, if we excite a set of spins in a plane and then acquire a signal from that plane a time, Δ, later, the signal will be reduced in the positions at which the fluid has moved fastest, i.e. the excited spins will have moved out of the image plane to be replaced by fast moving spins that have moved into the image plane during Δ; these spins will not have received the initial excitation and therefore will not give any signal upon data acquisition. There are many variants of this approach (e.g. Pope and Yao, 1993b) but the principle remains the same. Because these methods rely on image intensity to determine the fluid velocity, calibration is necessarily relaxation dependent and quantification can be difficult. An extension of this approach is the Delays Alternating with Nutations for Tailored Excitation (DANTE) method, in which a grid of spins is excited in the imaging plane and

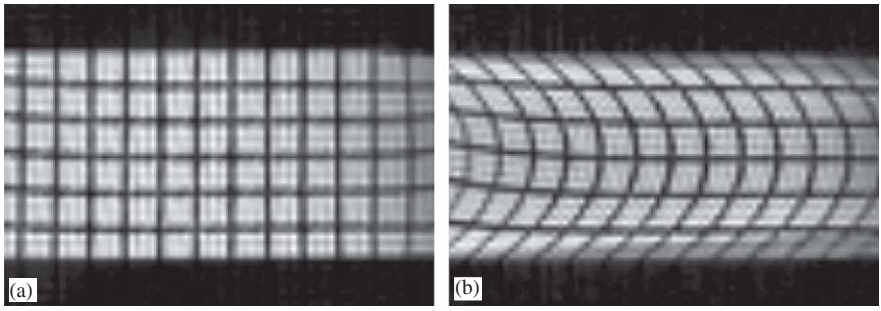

FIG. 10. Example of a DANTE-type velocity image. ^{1}H 2-D image of a 2.0 mm thick longitudinal slice at (a) zero flowrate of water and (b) a flowrate of 486 cm^3/min. Flow is from left to right.

the motion of the spins observed at a later time (Mosher and Smith, 1990). An example of a DANTE-TOF image of laminar flow in a pipe is shown in Fig. 10.

D. TEMPERATURE

Temperature can be mapped by its effect on nuclear spin relaxation (Doran *et al.*, 1994; Jezzard *et al.*, 1992), resonance frequency (usually termed "chemical shift") (Bertsch *et al.*, 1998; Hall *et al.*, 2001) and diffusion (Le Bihan *et al.*, 1989). Because temperature influences so many MR characteristics of a system, great care must be taken to ensure that the effect on the MR signal that we assign to temperature is influenced only by temperature or that other influences can be quantified and hence "deconvolved" from the temperature measurement. For example, if a chemical reaction occurred within the sample of interest, the chemical shifts of the individual chemical species may be modified slightly by the change in mixture composition as well as by temperature variation within the sample. However, careful studies have been performed, and MR offers the opportunity for non-invasive temperature measurement. A recent review of this field has been given by Nott and Hall (1999). Figure 11 shows an example of temperature mapping reported by Bows *et al.* (2001) that compares 3-D temperature maps with maps of structural heterogeneity within a jar containing soup and meat balls.

E. THE *k*-SPACE RASTER

While the simple schematic of Fig. 4 allows us to appreciate the concept of obtaining spatial resolution in the measurement, it is almost impossible to understand and design MRI pulse sequences using this approach. Instead, the approach used is that of the so-called **k**-space raster, introduced by Mansfield (1977).

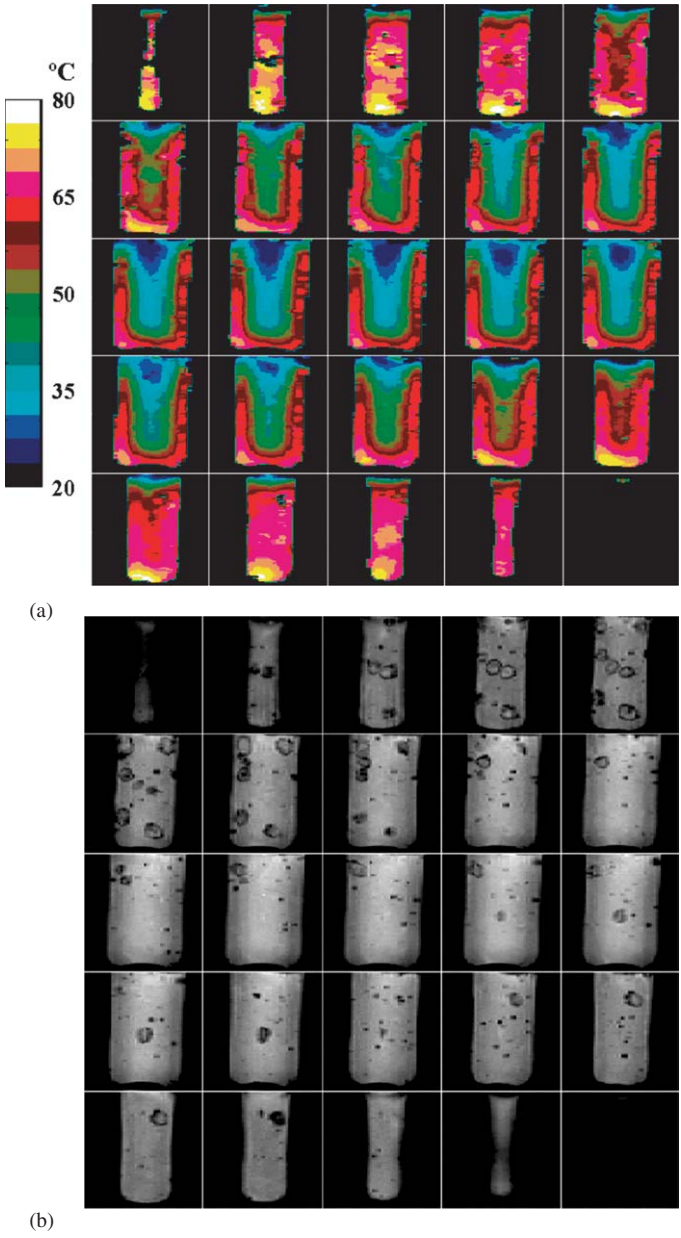

FIG. 11. 3-D (a) temperature and (b) spatial heterogeneity images of a 500 cm^3 jar containing soup with meat balls that has been immersed into a water bath between 95 and 98 °C for 11 min, displayed as a set of 2-D sections. Spatial resolution is 0.78 mm (along cylindrical axis) × 3.13 mm × 3.13 mm. Reproduced with permission from Bows *et al.* (2001).

Re-writing Eq. (2) for the general case of the variation of resonance frequency with spatial position **r**:

$$\omega(\mathbf{r}) = \gamma(B_0 + \mathbf{G} \cdot \mathbf{r}) \tag{17}$$

and neglecting the influence of relaxation on signal intensity, the transverse magnetization—and therefore the acquired signal, dS—in an element of volume d**r** at position **r** with spin density $\rho(\mathbf{r})$ is given by

$$\mathrm{d}S(\mathbf{G}, t) = \rho(\mathbf{r})\ \exp[\mathrm{i}\omega(\mathbf{r})t]\ \mathrm{d}\mathbf{r} \tag{18}$$

Inserting Eq. (17) into Eq. (18) gives

$$\mathrm{d}S(\mathbf{G}, t) = \rho(\mathbf{r})\ \exp[\mathrm{i}(\gamma B_0 + \gamma\mathbf{G} \cdot \mathbf{r})t]\ \mathrm{d}\mathbf{r} \tag{19}$$

A transformation into the rotating frame of reference allows us to re-write Eq. (19) as

$$S(t) = \iiint \rho(\mathbf{r})\ \exp[\mathrm{i}\gamma\mathbf{G} \cdot \mathbf{r}t]\ \mathrm{d}\mathbf{r} \tag{20}$$

Mansfield and Grannell (1973) simplified the interpretation of Eq. (20) and the development of imaging pulse sequences by introducing the concept of **k**-space, where the **k**-space vector is defined as $\mathbf{k} = (\gamma\mathbf{G}t/2\pi)$. It follows that Eq. (20) can now be written in terms of the **k**-space vector as

$$S(\mathbf{k}) = \iiint \rho(\mathbf{r})\ \exp[\mathrm{i}2\pi\mathbf{k} \cdot \mathbf{r}]\ \mathrm{d}\mathbf{r} \tag{21}$$

and the spatial distribution of spins is given by the inverse 3-D Fourier transform:

$$\rho(\mathbf{r}) = \iiint S(\mathbf{k})\ \exp[-\mathrm{i}2\pi\gamma\mathbf{k} \cdot \mathbf{r}]\ \mathrm{d}\mathbf{k} \tag{22}$$

Thus, the imaging experiment is seen as acquisition of data in the time domain and the sampling of the **k**-space raster, followed by Fourier transformation to the frequency domain, which in turn is directly related to real space. An imaging sequence can now be understood. Figure 12 shows a schematic of a simple 2-D imaging sequence. In this case let us assume that the sample is cylindrical and oriented along the z-axis, and an xy image is to be recorded. The first component of the pulse sequence is the so-called ''slice selection'' phase. This comprises the application of a narrow band r.f. excitation simultaneously with a magnetic field gradient imposed along the direction in which the 2-D image is to be taken (i.e. along the z-direction). The effect of this is that the only spins that will be excited will be those that resonate within the bandwidth $\Delta\omega$ of the r.f. pulse, and therefore only those spins that lie within a certain ''image slice thickness'' Δz. The rest of the sequence acquires data along a separate row of

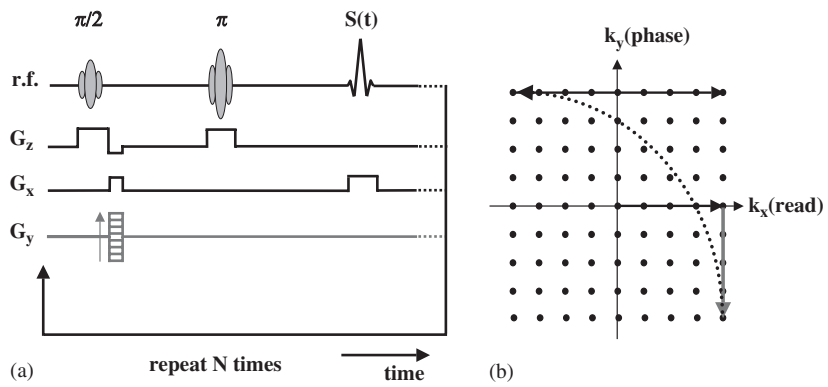

FIG. 12. (a) Schematic of a simple slice selective 2-D spin-echo pulse sequence. In this pulse sequence the magnetic field gradient is varied for successive acquisitions of different rows of the **k**-space raster. (b) The corresponding **k**-space raster used to show how we interpret the pulse sequence. Following a sufficient T_1-relaxation period the sequence is repeated to acquire a second row of the **k**-space raster. Acquisition of each row of **k**-space requires a separate r.f. excitation and application of a G_y-gradient of different magnitude.

the **k**-space raster for successive r.f. excitations. With reference to Fig. 12, a magnetic field gradient is first applied in the *x*-direction, simultaneously with the maximum magnitude negative magnetic field gradient in the *y*-direction. A slice selective π "re-focusing" pulse is then applied; this is represented on the **k**-space raster as a move from $k_{x,\max}$, $-k_{y,\max}$ to $-k_{x,\max}$, $k_{y,\max}$. A second gradient is applied along the *x*-direction while data, typically 128 or 256 complex data points, are acquired at a specified digitisation rate. The signal, $S(t)$, that is acquired during application of the second *x*-gradient is said to be frequency-encoded, since the signal is acquired in the presence of a magnetic field gradient. This gradient along the *x*-direction is therefore referred to as the frequency-encoding gradient and is also termed the "read" gradient. The acquisition of complex data points in the presence of a constant linear "read" gradient yields a straight line **k**-space data trajectory whose direction is defined by the Cartesian orientation of the gradient. A straight, equally spaced **k**-space trajectory will always result so long as the read amplitude gradient is kept constant and the digitisation (acquisition) rate of the complex data is fixed. The spin system is then allowed to return to equilibrium, via T_1 relaxation, and the pulse sequence repeated, this time with the second-largest negative *y*-gradient being applied, hence "reading" the next row of **k**-space. This process is repeated until the entire raster has been sampled. In this example, the gradient applied in the *y*-direction is referred to as the "phase encoding" gradient. Phase encoding refers to the action of an applied gradient that is responsible for moving the acquisition through the **k**-space raster. In this case, the action of the *x*-gradient is the same in each implementation of the pulse sequence, and it is the *y*-gradient that enables successive rows of **k**-space to be sampled. Therefore, if M complex points are

acquired along each row of **k**-space and N rows of **k**-space are sampled (i.e. there are N phase-encoding steps), the final data matrix will consist of $M \times N$ points on a rectilinear grid. A 2-D Fourier transform of these data followed by modulus correction gives a 2-D spin density map. 2-D images are acquired in typically a few minutes using this approach. While this might be considered slow, in that only pseudo-steady-state processes can be studied using this pulse sequence, it is robust in use and straightforward to implement. It is also easy to minimise, or at least account for, relaxation contrast effects within the acquired image.

F. Fast Data Acquisition

At the heart of recent developments in applying MR in chemical engineering research has been the implementation and further development of *fast* MR spatially unresolved and spatially resolved measurements. Recent implementations designed for specific applications in chemical engineering are described, with examples, in Section III. In this section, the principles of the three main strategies for fast MR imaging are described. We should note at this point that *fast imaging* (the term *fast* is used interchangeably with the terms *ultra-fast* and *rapid* both in this chapter and in the wider literature) is considered here to refer to the acquisition of, say, a 128×128 2-D image in less than 1 s. This section is not intended as a detailed review of fast-imaging strategies, but focuses specifically on those that are finding application in chemical engineering research rather than in the homeland of fast imaging, the field of medical imaging. While the data collection strategies will be similar in the medical and engineering fields, the physical and chemical nature of the samples to be studied and the nature of the data required are quite different; therefore, the details of the implementation will differ in terms of the hardware and the pulse sequences themselves. In using a fast sequence, we will often have to relax our desire for high spatial resolution ($\sim$15–30 μm) and take great care, if quantitative data are required, to account for relaxation contrast effects in the final image. Despite these additional considerations, in the hands of skilled users, these techniques are opening up a wealth of opportunities in chemical engineering research.

As we have seen, conventional spin echo imaging (Section II.E) typically takes approximately a few minutes because an independent r.f. excitation is required for acquisition of each row of **k**-space data. Hence, sampling of the complete raster is limited by the repetition/recycle time of the pulse sequence used, which in turn is governed by the inherent T_1 relaxation time(s) of the system under study. In general, the acquisition speed of an MR image may be improved by two basic methods:

(i) The sampling of more than one line of **k**-space for each r.f. excitation of the spin system
(ii) The use of rapid multiple r.f. excitations (and subsequent acquisitions).

Three sampling strategies will now be introduced: echo planar imaging (EPI), rapid acquisition with relaxation enhancement (RARE) and low excitation angle imaging (e.g. flash low angle shot (FLASH). The first two are based on the sampling of more than one line of **k**-space for each r.f. excitation, while the third uses rapid multiple r.f. excitations.

1. Echo Planar Imaging

The first example of rapid **k**-space imaging was demonstrated by Mansfield (1977), who realised that a complete image could be formed by the acquisition of multiple lines in **k**-space following a single r.f. excitation, in a technique today known as EPI. There are now many EPI-based sequences in use, mostly in the medical field. In chemical engineering research, while these methods acquire data faster than any other sampling strategy, their successful implementation is particularly sensitive to variations in magnetic susceptibility (i.e. gas/liquid/solid interfaces) within the sample. A common EPI sequence, known as Modulus Blipped Echo planar Single-pulse Technique (MBEST-EPI) or Blipped EPI (Howseman *et al.*, 1988), is shown in Fig. 13. Using this sequence, a 128×128 image would typically take 100–130 ms to acquire. In this sequence, a single r.f. excitation is used to sample the entire **k**-space raster. Following r.f. excitation, gradients simultaneously applied in the x- and y-direction take you to the bottom row of **k**-space, this row of data is acquired, and then a small (or ''blipped'') y-gradient takes you to the next row of **k**-space which is then read in the opposite direction and so on until the whole raster has been ''read''. Post-acquisition data processing techniques address the fact that alternate lines of **k**-space are read in opposite directions. The significant step forward made by Mansfield was that he saw it was possible to ''refocus'' the decaying

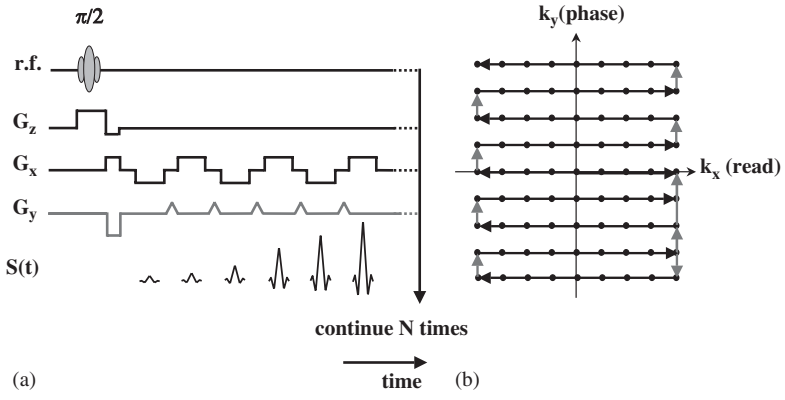

FIG. 13. MBEST-EPI: (a) slice selective pulse sequence and (b) corresponding **k**-space raster.

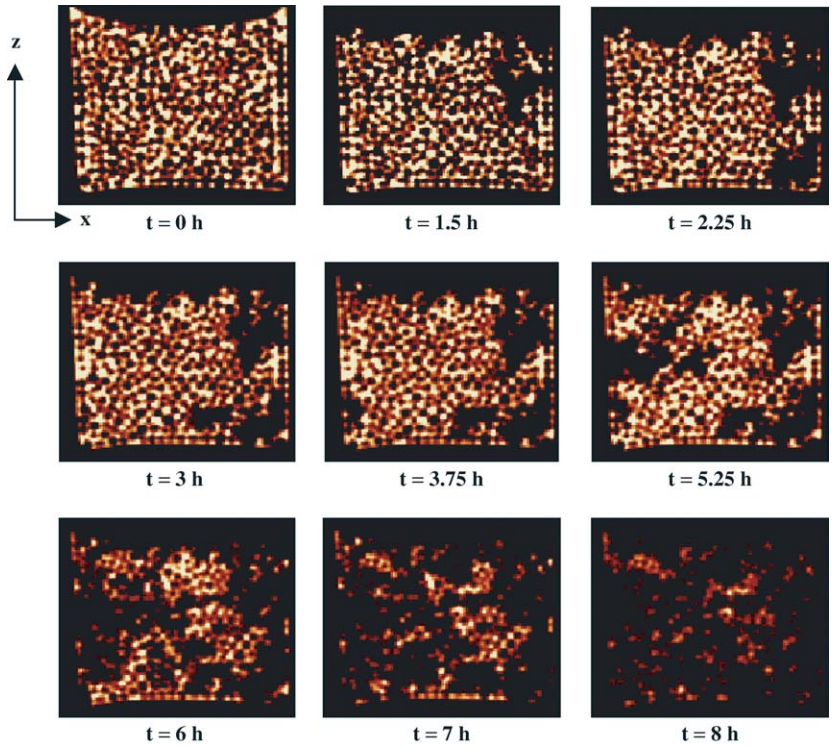

FIG. 14. 2-D slice sections through 3-D MR images of water distribution within an initially water-saturated packing of 500 μm glass spheres. Voxel resolution is 94 μm × 94 μm × 94 μm. Data are shown before drying commences and at 8 time intervals during the drying process. Only the water within the inter-particle space of the bead pack is imaged (white pixels). No signal is obtained from the solid and gas phases present.

magnetisation following r.f. excitation, using the concept of an "echo", so that it could be used to sample further lines of **k**-space (see Section II.B). Many variants of EPI exist; most of these have been developed with the aim of reducing potential artefacts in the image. Particular pulse sequences include radial EPI or REPI (Silva *et al.*, 1998), π-EPI or PEPI (Guilfoyle *et al.*, 1992) and Gradient and Spin Echo (GRASE) (Oshio and Feinberg, 1991). Manz *et al.* (1999b) have implemented an EPI-based sequence, which was sufficiently robust to spatially resolve drying within a packed bed of 100 μm glass spheres. Typical data are shown in Fig. 14; despite the drying process being characterised by a uniform water mass loss with time, the MR images clearly show the spatial heterogeneity in the drying process. This has been used to develop an invasion–percolation modelling strategy that predicts both the drying rate and the heterogeneity of the drying process (Gladden *et al.*, 2004).

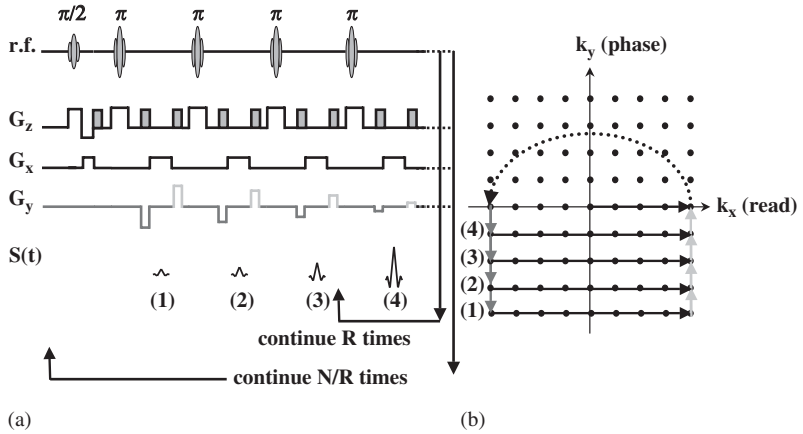

FIG. 15. **k**-space trajectory of a RARE sequence. The order of the phase encoding is shown by the numbers to the left of the raster. After each line in **k**-space is read the spins are returned to the same point on the $k_{x(\text{read})}$ axis prior to the application of the refocusing pulse shown by the dashed line and arrow.

2. *Rapid Acquisition with Relaxation Enhancement*

This type of image acquisition was first realised by Hennig *et al.* (1986), and variants such as turbo spin echo (TSE) and fast spin echo (FSE) exist. The **k**-space sampling strategy appropriate to RARE is shown in Fig. 15, and at first it might not seem different from the EPI approach; i.e. after acquisition of a single line in **k**-space the coherent signal is refocused and used to acquire further lines in **k**-space (or averages of the same line). However, there are important differences that make RARE much more robust (i.e. artefact-free) in application to systems characterised by heterogeneous magnetic susceptibility typical of those found in chemical engineering. Further, the decay of the MR signal in a RARE experiment is dependent on T_2 (and, of course, to some extent T_1) and not T_2^*, as is the case for EPI. In the magnetically heterogeneous systems of interest to us, T_2^* is considerably shorter than T_2; therefore, RARE allows us to acquire data of higher signal-to-noise over longer timescales, which is important if we wish to investigate the time–evolution of a system. An example of the application of RARE for rapid image acquisition is shown in Fig. 16, in which a single frame is shown from a series of 2-D images of an oscillatory chemical reaction occurring within a fixed bed. Relaxation contrast is used to discriminate between the reaction products Mn^{2+} and Mn^{3+} (Britton *et al.*, 2005). In this example, MR offers the opportunity to map the detailed structure of the fixed bed and the product distribution within it. This pulse sequence has also been recently applied to obtain quantitative images of the evolution of a lysozyme–urea separation within a chromatography column (Holland *et al.*, 2004).

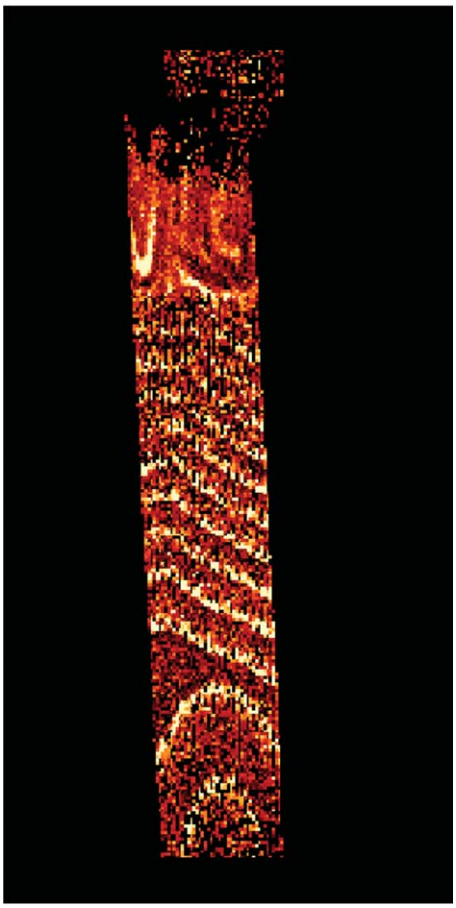

FIG. 16. 2-D MR image of an oscillating chemical reaction occurring within a bed of diameter 15 mm, packed with glass spheres of diameter 1 mm. In-plane resolution is 195 μm × 195 μm, and the image slice thickness is 1 mm. A single image was acquired in 1 s. Chemical waves are imaged as a result of the oscillatory production of Mn^{2+} and Mn^{3+} species; the location of Mn^{2+} and Mn^{3+} bands are identified as dark and light bands, respectively.

T_2- and T_1-relaxation contrast in the RARE acquisition is exploited such that the images are made selective to lysozyme and urea, respectively.

3. *Low Excitation Angle Imaging*

The important feature of this technique is that the r.f. excitations are characterised by a low flip angle, θ, typically 5–10°, in contrast to the $\pi/2$ pulse discussed in Section II.A. For this reason, this technique has been termed FLASH imaging or SNAPSHOT imaging (Haase *et al.*, 1986). The signal resulting from the small flip angle θ is proportional to $\sin\theta$, while the longitudinal (z-axis) magnetisation that remains after the excitation is

proportional to $\cos\theta$. Fractions of this remaining magnetisation are then used to sample successive lines of **k**-space. A 128×128 image based on a repetition time of 3 ms takes approximately 380 ms to acquire. The disadvantage of this approach is that by using only a proportion of the available magnetisation, signal-to-noise ratio in the image is significantly reduced. However, the important advantage is that the acquired signal is not strongly influenced by relaxation contrast effects or artefacts associated with molecular motion and magnetic susceptibility. In short, one is sacrificing temporal and, potentially, spatial resolution (i.e. signal-to-noise) for increased robustness in implementation.

There is no "rule" as to which fast-imaging technique should be used in a given application, and the following guidelines should be treated with caution. In short, the best approach is to implement each method and see which works best in a given application. EPI-based techniques are the fastest and can incorporate measurements of velocity vectors, but are also the most sensitive to variations in magnetic susceptibility within the sample. They are the most difficult to implement and in many circumstances cannot be used, as the resulting image contains obvious artefacts. FLASH/SNAPSHOT and RARE are, in general, slightly slower than EPI, but they are more robust, thereby making them more useful in day-to-day chemical engineering applications. The major differences between them are that they are influenced predominantly by different contrast mechanisms: RARE by T_2 and FLASH/SNAPSHOT by T_2^*. Thus, using the same argument as that used in comparing EPI and RARE previously, RARE will usually be the technique of choice. Further, RARE offers substantial signal-to-noise gains over FLASH/SNAPSHOT.

III. Recent Developments in MR as a Tool in Chemical Engineering Research

What constitutes an advance in any field will always be subjective. However, the combination of the inherent ability of MR methods to probe the internal structure and transport processes from the Å- to cm-scale phenomena non-invasively, quantitatively and with chemical resolution, and with the ability to acquire these data sufficiently fast so that unsteady state processes can be studied is undoubtedly going to open up new avenues of research and allow us to investigate many phenomena for the first time. This section summarises five recent developments in the field of MR in chemical engineering. The first four sub-sections (Sections III.A–III.D) report developments of fast MR measurement pulse sequences, which have recently been implemented for application in chemical engineering research. The final sub-section (Section III.E) addresses a new and different field of research, that of gas-phase imaging.

A. "Ultra-fast" Imaging of Velocity Fields

Imaging unsteady state or turbulent flow fields is a subject of long-standing interest in chemical engineering. Many experimental approaches have been used, including particle imaging velocimetry (PIV) and laser Doppler anemometry (LDA) techniques. The motivation for implementing MR flow measurement in this application is not only to allow us to study flow fields within optically opaque fluids, but also to extend the measurement to multi-phase, multi-component flows. In principle, as long as the MR pulse sequence can be made robust with respect to variations in magnetic susceptibility across phase boundaries, the measurement should be quantitative, regardless of the void fraction of any phase. In contrast to other methods, an image reconstruction algorithm is not required to take us from the acquired raw data to the final image: the only processing operation is a Fourier transform of the time-domain data. This should make MR much more quantitative in the sense that no corrections need to be considered for the scattering of probe radiation from interfaces within the sample. Fast MR techniques are now being applied to various topics in the field of fluid mechanics, including mapping spatio-temporal structures formed in Taylor Couette flow (Kose, 1994), and the velocity patterns within a falling liquid film (Heine *et al*., 2002) and a free-falling drop (Han *et al*., 2001a); this final example is particularly elegant (see Fig. 17). Sufficient signal-to-noise cannot be acquired from a measurement of a single falling drop; hence, data from multiple falling drops are acquired. This is achieved by releasing successive "identical" drops and gating the data acquisition such that data are acquired as each drop falls through the field of view of the imaging experiment.

Measurements of turbulent flows have been addressed previously by two MR methods: by measurement of signal attenuation and time-averaged velocity profiles. Kuethe (1989) reported the first imaging study of turbulent flow in which the flow was generated by a jet of water passing through a nozzle. In this study, a measure of turbulent diffusivity was obtained from a measurement of the signal attenuation observed in time-averaged images, employing the approach described in Section II.C. Similar approaches were later used by Gatenby and Gore (1994), employing a spatially unresolved diffusion measurement sequence to study pipe flow up to Reynolds numbers as high as 6270, and Kuethe and Gao (1995) to study pipe flows up to higher Reynolds numbers of 12000–58000. The alternative approach is that of Li *et al*. (1994), who reported time-averaged velocity measurements of flow in a cylindrical pipe; 1-D velocity profiles were measured for Reynolds numbers up to 9000. The results showed a correlation between the pixel intensity of the time-averaged flow image and the local turbulence intensity, with the latter showing good agreement with earlier data recorded using a hot-wire anemometer technique (Laufer, 1954). More recently, Han *et al*. (2001b) used an approach similar to that of Li *et al*. (1994) to investigate the non-Newtonian flow of blood in a pipe at Reynolds numbers up to 3500.

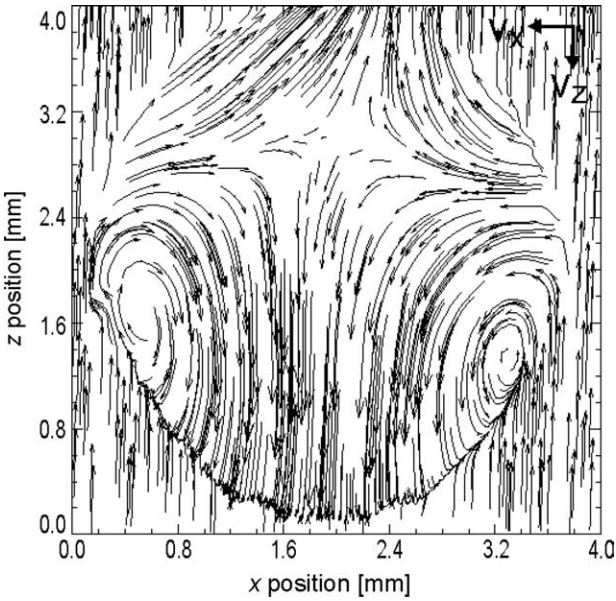

FIG. 17. Velocity components v_z, v_x are shown within a drop of pure water falling at 2.0 m/s as a function of position along the zx plane, averaged over the y dimension of the drop. The v_z component is scaled relative to the average falling velocity of 2.0 m/s. Reprinted with permission from Han *et al.*, (2001a). Copyright (2001), American Physical Society.

Neither of the two aforementioned methods directly measures the actual velocity vectors describing the flow field. In both cases even if an "excitation-acquire" sequence is fast, the data then have to be signal-averaged to provide adequate signal-to-noise in the final data set. In contrast, EPI (Section II.F) can be integrated with a transport measurement sequence (e.g. Fig. 7) to provide images of the flow field at timescales of ~30 ms or less. Kose (1991a,b, 1992) reported the first EPI-MR images of turbulent flow in which individual velocity vectors characterising the flow were resolved. In particular, the velocity distribution in a cross-sectional plane perpendicular to the direction of superficial flow at a Reynolds number of 2250 was imaged; clear visualisation of a turbulent "puff" was reported. More recently, the work of Kose has been extended to acquire images of three orthogonal velocity components from a single excitation over a timescale of 60 ms, with each velocity component itself being acquired in <20 ms. Alternatively, up to 16 velocity images can be acquired, at time intervals of 20 ms, from a single excitation. The maximum number of images acquired is limited by the residence time of the moving fluid within the imaging coil. These images were acquired in a 2-D data matrix of size 64×32 (Sederman *et al.*, 2004a). This is fast enough for the evolution of turbulent eddies in the flow to be followed. Acquisition of successive velocity images allows the acceleration field to be calculated. These data were acquired over a

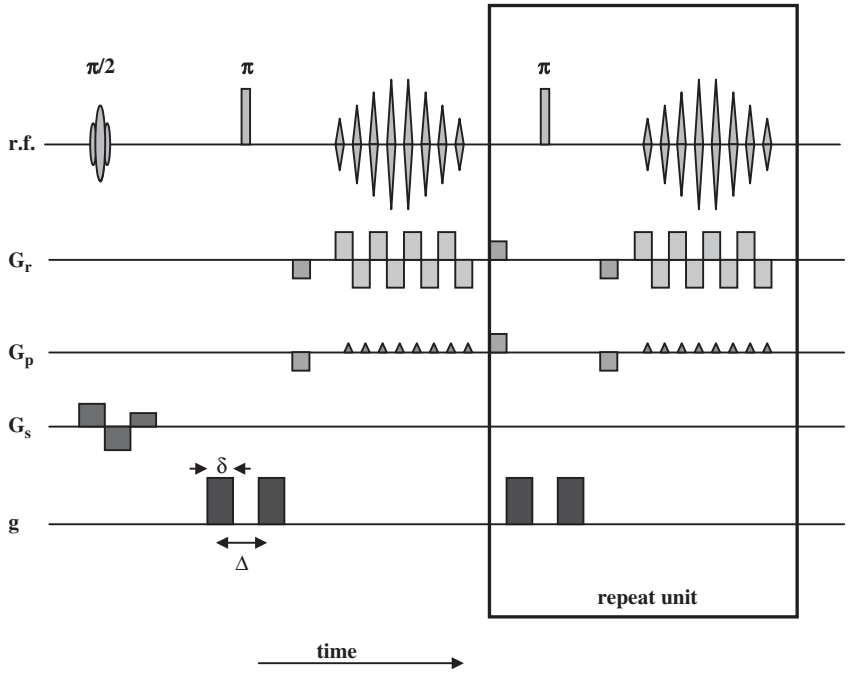

FIG. 18. Schematic of the GERVAIS pulse sequence, identifying all pulse and delay timings. The pulse sequence shown is that for acquisition of successive velocity images. The magnitude and orientation of the **g**-gradient are changed as determined by the velocity or acceleration vector that is to be measured.

wide range of Reynolds numbers encompassing the transition from pure laminar flow into the turbulent flow regime ($1250 < Re < 5000$). This pulse sequence has been named the gradient echo rapid velocity and imaging sequence (GERVAIS) and is based on the MBEST-EPI, or Blipped EPI, sequence (Section II.F), with the modification that after the initial excitation pulse, each image is preceded by a velocity-encoding gradient pair, separated by a π-refocusing pulse. The GERVAIS pulse sequence is shown in Fig. 18, and the basic combination of transport measurement gradient pair and EPI sequence is clearly seen with reference to Figs. 7 and 13. With reference to Fig. 18, velocities in the x-, y- and z-directions are acquired by changing the direction of the velocity measurement gradients (**g**). Figure 19 shows samples of these three Cartesian component velocity images for six different liquid velocities. The velocity component in the superficial direction (v_z) is given by the colour scale bar and the magnitude and direction of the transverse (v_x, v_y) velocity components are indicated by the vector arrows present on each of the images. More recently, the GERVAIS pulse sequence has been applied successfully to image unsteady-state flows in narrow fixed-bed reactors (Sains *et al.*, 2005).

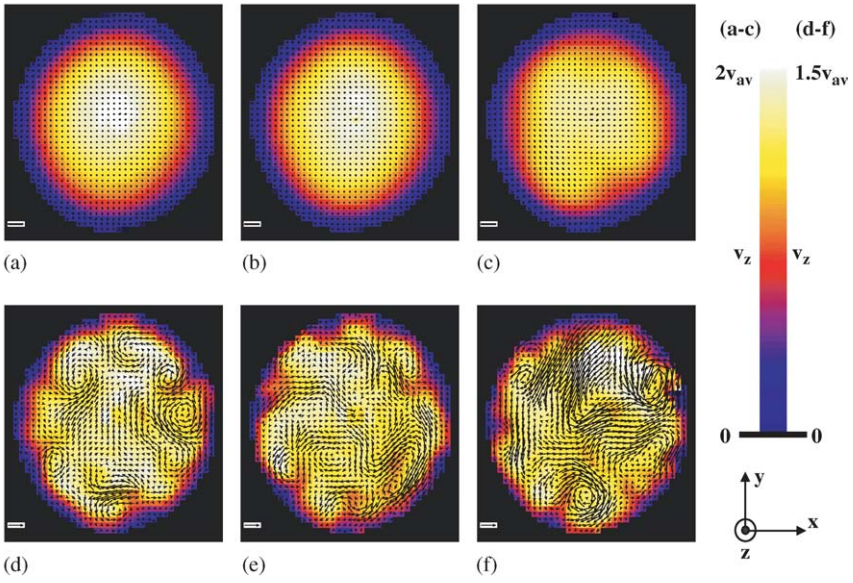

FIG. 19. Imaging unsteady state and turbulent flow of water within a 29 mm diameter pipe. Three orthogonal component velocity images acquired at increasing *Re* of (a) 1250, (b) 1700, (c) 2500, (d) 3300, (e) 4200 and (f) 5000 are shown. The colour scale identifies the magnitude of the *z*-velocity, and the flow velocity in the plane of the image (i.e. *x*–*y*) is shown by the vectors on each image. The vector scale bar on each image corresponds to 1 cm/s. Reprinted from Sederman *et al.* (2004a) with permission from Elsevier. Copyright (2004).

B. Multiple Images From a Single Excitation

As discussed in Section II.F, the RARE method is a particularly robust method for fast data acquisition in chemical engineering systems, which are often characterised by a range of magnetic susceptibilities. The resulting short nuclear spin relaxation times combined with rapid timescales over which a system may change impose far greater requirements on the imaging pulse sequence than are encountered when studying medical systems. Recently, a variant of RARE has been implemented (Sederman *et al.*, 2003) that yields *multiple images* from full **k**-space data at multiple echo times following a single r.f. excitation, not just a *single* complete image from a single excitation. This pulse sequence has been named single excitation multiple image RARE (SEMI-RARE) and is an extension of a standard RARE experiment. Implementation of SEMI-RARE allows the acquisition of up to ~120 images, in immediate succession, from a single excitation pulse. The actual number of images acquired from a single excitation is determined by the characteristic nuclear spin relaxation times of the system under study. A fine demonstration of the power of this technique is the visualisation of gas–liquid flow within the parallel channels of a ceramic monolith. To our knowledge MR is the only technique

that has been able to image non-invasively within such a ceramic monolith. This is also a good example of the robustness of the RARE methodology. Not only do we have varying magnetic susceptibility across the gas–liquid interface, we also have the interface of both with the walls of the ceramic channels. In this system, it is not practical to reduce the magnetic susceptibility variations between the gas and liquid by introducing chemical species that modify the magnetic susceptibility of the liquid phase, because such species will be adsorbed from the liquid onto the porous walls of the monolith. Thus, RARE is probably the only MR method that can be used in this application.

Figure 20 shows images, recorded in real-time using the SEMI–RARE pulse sequence, of gas flow through stagnant liquid within parallel-channel ceramic monoliths (Gladden, 2003; Gladden *et al.*, 2003b). The monoliths were of diameter 48 mm and length 0.15 m, contained within a Perspex column of inner diameter 50 mm. Gas (compressed air) was introduced at the base of the liquid (water) flooded column at flow rates of between 50 cm^3/min and 300 cm^3/min. In this experiment, four images were acquired in immediate succession from a single excitation. A single frame took 146 ms to acquire. The images are taken over a field-of-view of 50.6 mm × 50.6 mm, with an in-plane pixel resolution of 391 μm(x) × 781 μm(z). The centre of the imaging section was positioned at the centre of the monolith, i.e. 7.5 cm from the monolith outlet. The thickness of the image slice is 600 μm. Figure 20 shows the first (a) and second (b) images of a sequence of four taken after a single excitation. The orientation of the slice was selected to image just a single row of parallel channels within the monolith. The imaging resolution allows easy identification of the individual channels and several bubbles (zero signal intensity) can clearly be identified. From these images, gas-phase volume fractions and distributions of gas-bubble length and

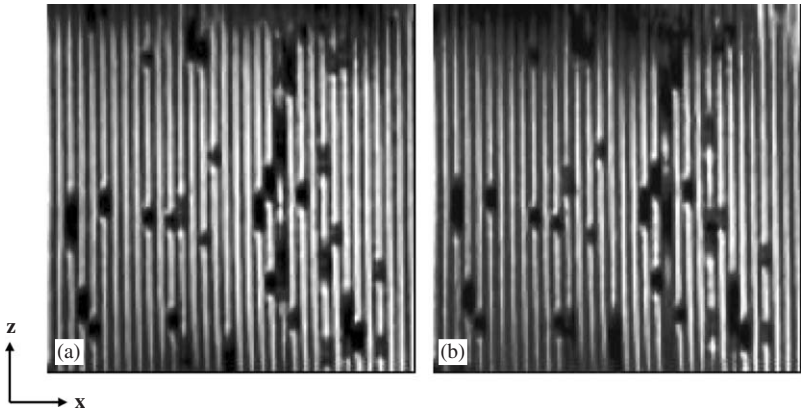

FIG. 20. Two successive 2-D xz images of two-phase flow through the parallel channels of a ceramic monolith rated at 400 cpsi, for a gas flow rate of 200 cm^3/min: (a) 74 ms after excitation (b) 220 ms after r.f. excitation. In-plane image resolution is 393 μm (x) × 783 μm (z). Reprinted from Gladden, (2003), with kind permission of Springer Science and Business Media.

velocity as a function of gas flow rate and channel size are obtained directly. In this particular example, monoliths rated at 300 and 400 channels per square inch (cpsi) were studied. Increasing the gas flow rate was seen to increase the number of large bubbles and the average bubble velocity. A bimodal distribution in the bubble velocities was observed for flow within the larger channel size (300 cpsi) in contrast to a broad unimodal distribution characterising two-phase flow within the smaller channel size (400 cpsi).

C. Imaging Rotating Systems

Albeit a technique with a niche application, this variant on the RARE methodology demonstrates the flexibility of MR to achieve specific measurements. The particular application for which this pulse sequence was developed was to avoid blurring of images recorded for systems rotating at a known, constant angular frequency. This RARE sequence with rotational compensation is shown in Fig. 21. It works by reorienting the direction of the imaging gradients between each cycle or echo acquisition, as shown schematically in Fig. 21b, to ensure that the **k**-space raster remains aligned with a chosen rotational velocity, ω. This means that the directions of the read and phase gradients rotate after each cycle or echo acquisition, but remain perpendicular to one another, their angle with the x-axis being α and $\alpha + \pi/2$, respectively. α increases with t, the time between successive echo acquisitions, by an amount ωt. With reference to Fig. 21b, note that unlike conventional RARE (see Fig. 15), the sequence begins and ends at the origin of **k**-space between each cycle or echo acquisition. This increases the robustness of the pulse sequence since the origin of **k**-space is the only point unaffected by the gradient rotation. In the laboratory frame this

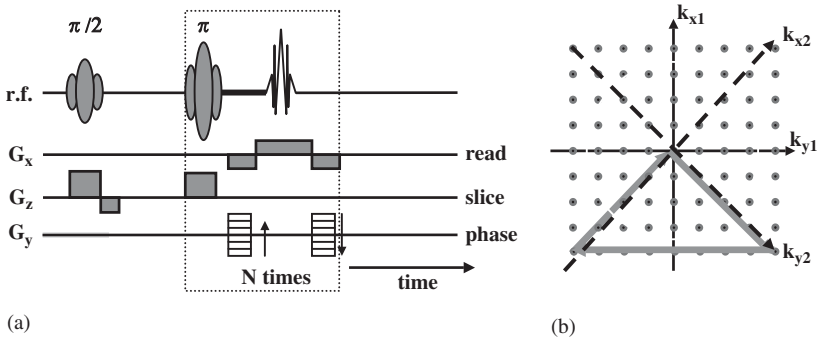

Fig. 21. (a) The "rotating RARE" pulse sequence, and (b) the associated **k**-space raster. The pulse sequence is a variant of the RARE pulse sequence with the read and phase directions rotated with respect to the laboratory-frame after each echo acquisition such that the orientation of **k**-space relative to the rotating object remains constant. After each echo acquisition, the system is returned to the centre of **k**-space, which is not affected by sample rotation.

corresponds to an irregularly sampled **k**-space raster; for a sample rotating at the pre-defined rotation rate this will correspond to the sampling of a rectilinear **k**-space raster.

Figure 22 shows a 2-D image of a paddle wheel rotating within a cylindrical vessel (Sederman *et al.*, 2004b). The paddle is rotating at an angular frequency of 1.6 rev/s and therefore appears blurred when acquiring the 2-D image with an acquisition time of 300 ms. By applying the rotational compensation, blurring is prevented. The particular application for which this pulse sequence was developed was to image accurate droplet shapes *in situ* during exposure of an emulsion to a shear field within a Couette cell. By allowing a given droplet to attain its equilibrium radial position within the Couette cell during shear, the rotational compensation is optimised for that particular angular frequency. Figure 23 shows the deformation of a water droplet in a 1000 cSt silicone oil solution under conditions of increasing shear within a wide-gap Couette cell. The droplet has zero intensity in this image since the image has been acquired under conditions of T_2 contrast such that signal is acquired only from the silicone oil. By measuring the short and long axis of the droplet as a function of rotation rate, standard analysis (Taylor, 1934) is used to obtain an *in situ* estimate of the interfacial tension characterising the system.

D. "Ultra-fast" Diffusion Measurement

The diffusion train (DIFFTRAIN) pulse sequence (Stamps *et al.*, 2001) is an elegant technique for fast measurement of PFG-MR (PGSE-MR) data, and finds application in the rapid measurement of, for example, emulsion droplet-size distributions or propagators. DIFFTRAIN speeds up the conventional ("slow") diffusion measurement experiment by using successive stimulated echoes from a single excitation pulse, such that a portion of the available magnetisation is recovered for each echo (cf. FLASH in Section II.F). Recently, DIFFTRAIN has been demonstrated in application to the determination of emulsion droplet-size distributions and propagators of water transport through a desalting column packed with Sephadex matrix (Buckley *et al.*, 2003). In both cases, the data were in quantitative agreement with data acquired using conventional "slow" techniques. In the case of the droplet-size distributions, data acquisition times were reduced from 10–20 min to 4 s, while in the propagator determinations, fast acquisition took less than 10 min, an order of magnitude faster than is the case with conventional PFG techniques. The reduction in measurement time for the emulsion droplet-size distributions means that it is now possible to follow the evolution of droplet size *in situ* during a mixing process. As long as signal-to-noise requirements are satisfied, there is no reason why these measurements cannot be integrated into an imaging strategy to obtain spatially resolved measurements of droplet size.

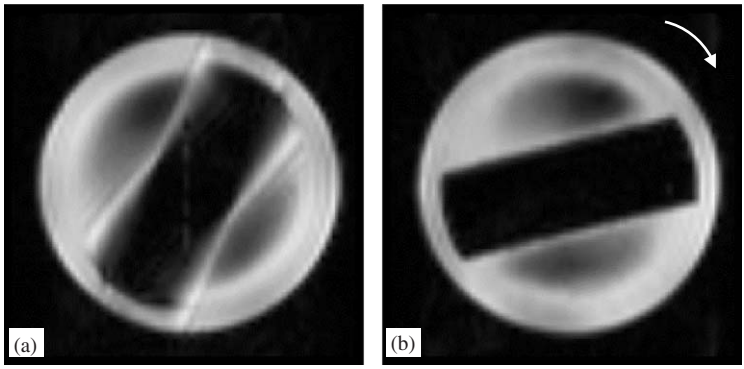

FIG. 22. (a) Conventional RARE and (b) "rotating RARE" images of a paddle rotating in water at 1.6 rev/s. Reprinted from Sederman *et al.* (2004b), with permission from Elsevier. Copyright (2004).

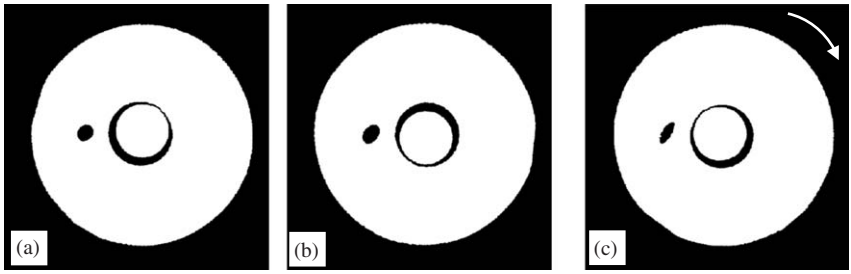

FIG. 23. Images acquired of 2 µl water droplets of 1% Tween 60 (w/w) with 0.005 M $MnSO_4$ in 1000 cSt silicone oil under shear rates of (a) 0.63 s^{-1} (b) 1.67 s^{-1} and (c) 3.25 s^{-1}. Water inside the rotating inner cylinder also appears in the images; it is off centre due to its chemical shift relative to that of the silicone oil. The figures have been rotated to show the droplets in the same position in the Couette. Reprinted from Sederman *et al.* (2004b), with permission from Elsevier. Copyright (2004).

E. GAS-PHASE MR

Both thermal and hyperpolarized gas-phase MR studies have until now predominantly addressed medical applications and, in particular, lung imaging. However, non-medical applications are now being reported. Conventional MR measurements rely on the "thermal" polarisation of the atomic nuclei within the magnetic field. Since the interaction energy of the nuclear "magnets" with the applied magnetic field is about 10^4 times smaller than the thermal energies of the system, the resulting polarisation of the nuclear magnets is very weak and the inherent sensitivity of MR measurements is therefore low compared to other spectroscopic techniques. This characteristic of MR measurements is

particularly limiting in studying systems of low nuclear spin density, such as gases. More recently, methods that enhance the signal available from gas-phase experiments by exposing the gas (usually ^{3}He and ^{129}Xe) to laser optical pumping have been developed. The population distribution between adjacent energy levels is thus modified, resulting in an increase in the polarisation of the nuclear spin system by 3–4 orders of magnitude, and a state of "hyperpolarisation" is reached. First, we will briefly review the current state of the art in using thermally polarised gases and then discuss the latest developments in using hyperpolarisation methods, focussing on non-medical applications.

Thermally polarised gas MR measurements have been successfully performed using ^{129}Xe and ^{19}F observation (for the case of the ^{19}F nucleus, the molecules CF_4, C_2F_6 and SF_6 are typically studied), and have been shown to be a powerful probe of inorganic porous media (e.g. rock cores), giving insights both to the structure of the porous medium and the transport of the gas within this structure (Bencsik and Ramanathan, 2001; Mair *et al*., 2002). As discussed by Mair *et al*. (2002), ^{3}He and ^{129}Xe are particularly well suited for such studies given their rapid diffusion, inert nature, low surface interactions (which reduces relaxation time effects) and the ability to tailor the diffusion coefficient by altering the gas pressure in the sample. In particular, the faster diffusivities of gas-phase species compared with liquid-phase probes of the pore space have made it possible to extend the length-scales that can be probed in porous media by more than one order of magnitude. However, in addition to the low signal-to-noise ratio associated with the low polarisation of the spin system, a further challenge in using gas-phase MR is that the T_2 of the gases is often very short. Kuethe *et al*. (2000) have made advances in using thermally polarised gases by developing hardware that recovers from the transmitter pulse rapidly enough to detect gases characterised by rapid T_2 relaxation times as short as $\sim$1 ms. This is a significant advance, since the combined effect of decreased signal loss due to the rapid switching times and the ability to perform rapid signal averaging now allows images of good quality to be obtained. Although originally developed for medical applications, the method has been successfully applied to the imaging of porous glasses and ceramics. Particularly noteworthy has been the extension of the method to map the specific surface area and trends in the local adsorption energy within these porous materials. This is done by exposing the porous sample to a gas at a range of gas pressures, and acquiring a spin density image at each pressure condition. In this way a spatially resolved Brunauer-Emmett-Teller (BET) isotherm has been generated (Beyea *et al*., 2002).

More recent studies of gas-phase imaging with more direct relevance to chemical processing and reaction engineering have involved the examination of thermally polarized gas (and liquid) flow in monolithic catalysts. Koptyug *et al*. (2000a) have obtained quantitative, spatially resolved velocity maps for the flow of thermally polarized acetylene, propane, butane and water flowing through the channels of alumina monoliths with an in-plane spatial resolution of 400 μm. The monoliths had a channel cross-section of 4.0 mm^2 and a wall channel

thickness of 1.0 mm. Axial gas-phase velocities of up to 0.93 m/s ($Re = 570$) were studied. The flow maps showed a highly non-uniform distribution of shear rates within the individual monolith channels. In a follow-up study, Koptyug *et al.* (2001) reported images of both liquid and gas flow and mass transport phenomena in two different cylindrical monolith catalysts (one with triangular channels, the other with square channels) at different axial locations within the monolith.

The advent of hyperpolarized ^{3}He and ^{129}Xe for use in MR studies has given further impetus to gas-phase studies. Brunner *et al.* (1999) have described a continuous flow system that circulates laser-polarised ^{129}Xe through the sample, yielding an enhancement of signal intensity of 3–4 orders of magnitude compared to the equilibrium ^{129}Xe signal. Gas flow displacement profiles of ^{129}Xe flowing through polyurethane foams of different densities and pore sizes were reported. Another exciting area of potential development is the use of laser-polarised gases to provide enhanced sensitivity to study species at surfaces (Pietraβ *et al.*, 1998). Exploitation of laser-polarised gases is also finding application in so-called "remotely detected MRI". A good description of this has been given by Seeley *et al.* (2004). The principle behind the measurement is easy to understand although the concepts are hard to grasp for those not well acquainted with MR. The key feature of remote detection is the spatial separation of the MR encoding and detection steps, which allows for their separate optimisation by providing the most suitable conditions for encoding without compromising detection quality. This is achieved by employing a "signal carrier" to encode MR information indicative of its environment. Time-domain (or **k**-space) information is stored point-by-point as spin polarization in the encoding location, each point being subsequently transported to the detection location. Remote detection is an indirect detection technique that exploits the principles of phase encoding. The resulting phase acquired after each signal acquisition provides one point in the indirect signal. In such a "remote" experiment, the indirect dimension provides information about the encoding environment, while the direct dimension gives the signal of the sensor in the detection region. In principle, this methodology can be extended to the "signal carrier" being water and oil—of particular relevance to, say, understanding oil recovery processes; the T_1 of these fluids currently limits their use in this application. In contrast, laser-polarised ^{129}Xe has a range of particular attributes, the most obvious being that it is a highly polarisable and chemically inert noble gas with a long T_1, and therefore acts as a very efficient carrier of the spin polarisation. Further, its wide chemical shift range makes it a powerful sensor of its local environment and therefore provides a wealth of physicochemical and biomedical information. To date, clear demonstration of enhanced signal-to-noise for indirect over direct detection has been demonstrated for a model porous medium comprising a 14-mm-diameter "honeycomb" phantom with 1.4-mm-diameter pores. There remains much work to do in optimising this experiment and in quantifying the effect of contrast mechanisms on the acquired

image, but the approach may offer opportunities to study systems inaccessible to more conventional MR measurement.

IV. Reaction Engineering: From Catalyst to Reactor

The following section does not dwell on the details of any of the MR techniques used, but brings together the various ways that MR can characterise and give insight into a particular field of chemical engineering–in this case, heterogeneous catalysis. As will be demonstrated, MR makes contributions to our understanding of a system from the size scale of the active site of the catalyst to the macroscopic phase distributions within a fixed-bed reactor. Inevitably, the examples are not exhaustive, and for the sake of continuity between examples, the majority are drawn from research in our own group. It is hoped that the reader, armed with knowledge of the examples cited in earlier sections that draw on applications in various fields of chemical engineering, will be able to identify applications of MR over various length-scales in their own field of interest.

A. MR Spectroscopy of Catalysts

In most cases reported in the literature, studies of the catalyst are performed on the as-prepared catalyst in powder form. It is important to remember that such characteristics may be modified when the catalyst is formed into the pellet for process operation. The motivation for current studies in the field of MR spectroscopy of catalysts is to characterise the active catalytic site and, in some cases, to study how reactant/product molecules interact with it. For these reasons this research remains predominantly in the area of mainstream chemistry research. However, it is quite likely that as chemical engineers engage with MR methods, there will be increasing interest in probing the catalyst structure and chemical processes occurring within the catalyst as part of understanding and optimising the overall catalyst/reactor system. An area that has already been taken up by chemical engineers is the study of molecular diffusion within catalysts. This will be described briefly in this section and then considered further in Section IV.B, where we discuss studies of molecular diffusion within catalysts at the length-scale of the formed catalyst typical of those manufactured for supported-metal catalysis.

With respect to *in situ* spectroscopy, there is no attempt here to give a detailed overview of the ongoing activities in this field. The interested reader is directed to excellent articles describing applications of MR spectroscopy in catalysis that have been published elsewhere (Baba and Ono, 1999; Dybowski *et al.*, 1991; Fraissard, 1999; Haw, 1999; Hunger and Weitkamp, 2001; Packer, 1996; Parker 2000; Roe *et al.*, 1998; van der Klink, 2000). Instead, we focus on the nature of

the information obtained and cite some illustrative examples in the respective fields.

1. Characterisation of Surface Chemistry

MR spectroscopy is widely used to study the surface chemistry of catalysts and the interaction of the surface with reactant and product species, as well as investigating the role of surface modifiers to be exploited in catalytic reactions. For example, ^{27}Al and ^{31}P solid-state MR spectroscopy have been used to study the acidity and surface structure of aluminas subjected to a fluorination treatment (Chupas and Grey, 2004). In this study, ^{27}Al was used to show the preferential removal of 5-coordinate aluminium sites during fluorination, suggesting that they are predominantly localised near the surface. The sorption of basic phosphines as probe molecules for acid sites coupled with ^{31}P-MR was used to follow the changes in acidity after fluorination of the surface. Zhang *et al.* (2000) have used MR to probe the adsorption of SO_3 onto oxide surfaces.

2. Characterisation of Coke

^{13}C-MR spectroscopy and related techniques has been established as a technique for characterising the carbon-to-hydrogen ratio of carbonaceous residues on the catalyst surface (Duncan *et al.* 1985, Egiebor *et al.*, 1989; Groten *et al.* 1992). MR spectroscopy continues to be used in this way, but is more often used in combination with other characterisation techniques such as X-ray diffraction, electron spin resonance, infra-red spectroscopy and temperature-programmed oxidation studies, to gain information on the structure, carbon-to-hydrogen ratio and combustion behaviour of the coke (Martin *et al.*, 2004; Wang *et al.*, 2001).

3. MR Spectroscopy Studies of In Situ Reactions

A review of this field has been given by Haw (1999). Reactions can be followed either in sealed glass ampoules or flow-through cells constructed within the spectrometer. The formation of intermediates can be studied in real time. An elegant example of this was shown in an early study of methanol to gasoline conversion over HZSM-5 zeolites. As a result of the shape selectivity of the catalyst, spectroscopic evidence of reaction intermediates, which were not seen as reaction products, was observed (Anderson and Klinowski, 1990).

4. Molecular Diffusion within Catalysts

Most studies of molecular diffusion within catalysts have been performed on the as-prepared (i.e. powder form) of the catalyst and focus predominantly on zeolites and related catalytic materials. A recent review of this field has been given by Karger and Freude (2002). *In situ* studies of molecular diffusion during reaction include ^{13}C-PFG-MR studies of diffusion and reaction of isopropanol

in zeolite CsNaX (Schwarz *et al.*, 1995), intracrystalline diffusion during isopropanol conversion in X-type zeolites (LiNaX, CsNaX and NaX) (Schwarz *et al.*, 1997) and molecular diffusion during catalytic reaction of cylopropane to propene in zeolite X (Hong *et al.*, 1992).

B. Micro-imaging and Molecular Diffusion Studies of Formed Catalyst Pellets

The majority of the early MR imaging studies specific to catalysis addressed the heterogeneity in structure and transport within catalyst pellets. In-plane spatial resolution was ~30 μm, and the pellets themselves were typically 1–5 mm in size. In the majority of cases, studies have addressed the pure, usually oxide, support so that the quantitative nature of the data obtained is not sacrificed by the presence of metal, which can introduce an unknown extent of nuclear spin-relaxation time contrast into the images.

1. Structure-Transport Relationships

By working with typical spatial resolutions of ~30–50 μm, individual pores within the material are not resolved. Further, the transport characteristics within small pores (e.g. nanopores) may not contribute to the measurement owing to the very short relaxation times of fluid contained within such pores. However, a wealth of information can be obtained at this lower resolution. Typical data are shown in Fig. 24, which shows images or maps of spin density, nuclear spin-lattice relaxation time (T_1) and self-diffusivity of water within the porous pellet (Hollewand and Gladden, 1993). In-plane spatial resolution is 45 μm × 45 μm, and the image slice thickness is 0.3 mm. The spin density map is a quantitative measure of the amount of water present within the porous pellet, i.e. it is a spatially resolved map of voidage. Estimates of voidage obtained agree to within 5% of those obtained by gravimetric analysis. The spin-lattice relaxation time map (as discussed in Section II.B) yields information on the spatial distribution of mean pore size within a given image pixel. Lighter shades in the image correspond to larger mean pore size. Even at this course resolution, these data give us additional insight to that which may be obtained from a 1-D pore-size distribution obtained by, for example, mercury porosimetry or nitrogen adsorption measurement. Thus, by using MR, we can now probe the spatial heterogeneity in porosity within a catalyst pellet that will have been introduced during the manufacturing process. Figures 24a and b allow us to discriminate between a region of given voidage comprising many small pores or a single large pore. The structure–transport relationship characteristic of the catalyst pellet is seen in comparing Fig. 24b and c; i.e. the spatial heterogeneity in variation of D values is much more consistent with the heterogeneity in the intensity seen in the T_1 maps as opposed to the spin density maps. Thus, we conclude that it is the

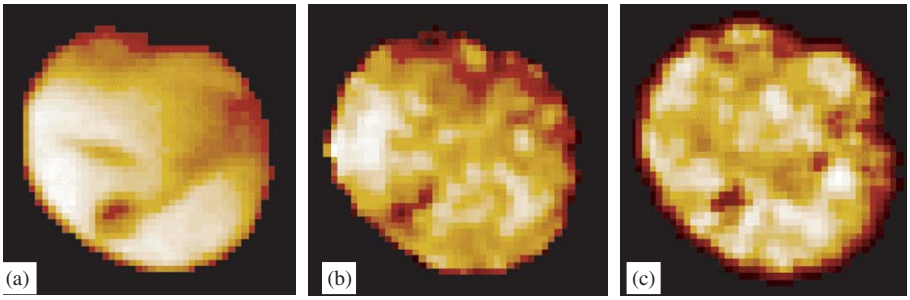

FIG. 24. Spin density, T_1 and water diffusion images for a 2.2 mm diameter, spherical silica catalyst support. In-plane pixel resolution is 45 μm × 45 μm; image slice thickness is 0.3 mm. (a) Spin density map; lighter shades indicate higher liquid content. (b) T_1 map (150–400 ms); lighter shades indicate longer values of T_1. (c) Diffusivity map (0–1.5×10^{-9} m^2/s); lighter shades indicate higher values of water diffusivity within the pellet.

spatial variation of local pore size that has the dominant influence on molecular transport within the pellet. There have been a number of studies exploiting this type of MR measurement. For example, water spin density imaging has been used to explore the 3-D structure of activated alumina spheres. The spheres were observed to exhibit a uniform ball structure comprising spherically layered structures and voids (Timonen *et al.*, 1995).

Simple spin-density imaging has also been used to characterise the tortuosity of catalyst pellets manufactured in different ways (Rigby *et al.*, 1996). This is achieved by initially impregnating the catalyst with deuterated water (invisible to a ^{1}H-MR experiment) and then immersing it in normal, protonated water. The diffusive exchange of ^1H_2O with ^2H_2O within the pellet is followed by ^{1}H imaging. The resulting time-resolved ^1H_2O concentration profiles are then fitted to a standard diffusion equation and the effective water diffusivity and, hence, catalyst tortuosity, are obtained. Measurements of this type are straightforward to perform and give immediate insight into transport anisotropies within the catalyst resulting from manufacturing process parameters.

When originally recorded, the types of images shown in Fig. 24 suggested a potential dilemma in using this type of information to aid the development of modelling the structure of catalyst pellets and the transport processes occurring within these porous structures. Each pellet that is imaged, even if taken from the same batch, will yield a different image. However, we know that a given batch of pellets is expected to have consistent (i.e. ''typical'') properties ''in-use''. In studying the spin density (voidage) and spin-lattice relaxation time maps of many pellets it was found that the heterogeneity in pore size, as characterised by the fractal dimension of the T_1 map, was consistent between images of pellets drawn from the same batch (Gladden *et al.*, 1995). The fractal dimension of these images actually identifies a constant perimeter–area relationship for clusters of pixels of similar intensity (i.e. pore size) in the image. The most obvious

physical interpretation of this is that a given manufacturing process imposes a particular meso-scale (0.1–1 mm) structure characterising the spatial distribution of pore sizes within the pellet.

Numerical modelling strategies employing simulation lattices constructed to have the same fractal dimension as that obtained from the MR images have had some success in predicting mass transfer characteristics in porous catalyst supports (Rigby and Gladden, 1998). Current strategies include combining the characterisation of meso-scale structure obtained from MR with characterisation of the micro-pore structure obtained by, say, nitrogen adsorption or mercury porosimetry to construct hierarchical models of the micro- and meso-length scales that control transport processes (Rigby and Daut, 2002; Rigby and Gladden, 1999).

2. *Catalyst Preparation*

The ability to image liquid distribution in catalyst support pellets suggests immediate applications in investigating transport processes occurring during catalyst manufacture and, in particular, wet impregnation methods. Aspects of catalyst preparation that MR has been used to address include both liquid and ion migration process. Early work demonstrated the ability of 2-D MR images to discriminate between so-called uniform and capillary-controlled drying models (Hollewand and Gladden, 1994). The dominant drying mechanism was shown to be dependent on the timescale over which drying was performed. Further, for those systems for which a capillary-controlled drying mechanism was identified as appropriate, a simple numerical simulation of the drying process provided an estimate of the mean co-ordination number associated with a random pore network describing the micro-pore structure of the material. Network connectivities estimated in this fashion were consistent with those estimated from mercury porosimetry analysis.

Detailed studies of 1-D ^{1}H imaging of alumina and titania cylinders (of length 1.2 cm and diameter 3.6 mm) have been reported by Koptyug and co-workers (Koptyug *et al.* 1998, 2000b) in which consideration of relaxation time effects on the water concentration profiles are discussed. These porous catalyst supports were impregnated with acetone, benzene, cyclohexane and water, and the drying of these liquids was monitored under different drying conditions, i.e. different nitrogen flow rates. The 1-D profiles were able to discriminate fast- and slow-drying regimes. The detail of the water concentration profiles as a function of time were found to be sensitive to the pore-size distribution of the catalyst support. A numerical analysis of the quantitative liquid concentration profiles was performed by fitting the profiles to the diffusion equation, allowing for a concentration-dependent diffusivity. It was shown that for liquids characterised by low surface tension, such as acetone, benzene and cyclohexane, transformations of the concentration profiles could be adequately modelled assuming a

liquid-independent diffusivity. In contrast, the diffusivity of water in both titania and alumina pellets substantially decreased as a function of water content.

MR imaging has also been demonstrated to be a potentially useful tool for characterising metal-ion distribution within catalyst pellets, both in a static state and as an *in situ* measurement during catalyst synthesis. Khitrina *et al.* (2000) have exploited the effect of relaxation time contrast within images to map out the metal-ion distribution. It is non-trivial, and it has not yet been attempted to make such measurements quantitative, but the method does provide a non-destructive way of identifying the position of metal bands within the catalyst that is consistent with the position identified by an electron probe micro-analyser. The approach uses ^{1}H micro-imaging to follow the distribution and spin-lattice relaxation time of cyclohexane within the catalyst. Cyclohexane species interacting with the hexachloroplatinate dianion during the timescale of the measurement are associated with an increased spin-lattice relaxation time; therefore, T_1-maps of the sample identify the location of the hexachloroplatinate dianion within the porous catalyst support. This methodology has been used to follow the dynamics of hexachloroplatinate dianion re-distribution during a competitive impregnation of the support with an aqueous solution of $H_2PtCl_6 + H_2C_2O_4$. It is seen that after 5 h of impregnation, the egg-white-type profile transforms into a classic egg-yolk profile.

At a slightly larger length-scale we can also follow in real time the water loss during drying from liquid-saturated arrays of particles, as was shown in Fig. 14. Although this work was originally undertaken to investigate product heterogeneity arising from a different particle-drying process, this experimental configuration has immediate relevance to catalyst synthesis in the context of the drying of a batch of catalyst pellets following a wet impregnation synthesis (Gladden *et al.*, 2004).

3. *Reaction*

This is an area in which there is likely to be considerable future interest. Of course, apart from the challenge of being able to measure species-dependent profiles within the pellet, we need to think carefully about how these data will be used. To date, images of liquid distribution during chemical reaction within a cylindrical Pt/γ-Al_2O_3 catalyst pellet (diameter and height 4.7 mm) have been reported (Koptyug *et al.*, 2002). In-plane spatial resolution was 230 μm × 140 μm, with an image slice thickness of 2 mm. A stream of hydrogen gas heated to 67–69 °C and saturated with α-methylstyrene vapour was supplied to the pellet at a flow rate of 18.5 cm^3/s. ^{1}H images of the evolution of the liquid distribution within the pellet were recorded during α-methylstyrene evaporation accompanied by its vapour-phase hydrogenation. To date there have not been any reports of chemically resolved images within individual supported-metal catalyst pellete—the ^{1}H signal in the previous example did not differentiate between reactants and product species. This is because of the severe line

broadening that occurs in the ^{1}H-MR resonances associated with individual molecular species when these molecules interact with the surface of the catalyst, causing a reduction in the relaxation times of those species which, in turn, is manifested by an increased line width in the frequency spectrum. However, this is not necessarily an insurmountable problem. Judicious selection of reaction systems may identify specific systems in which the relevant ^{1}H resonances can be discriminated. Alternatively, imaging of nuclei other than ^{1}H may provide the solution—^{13}C is an obvious choice. While the sensitivity of a ^{13}C measurement is substantially less than that of a ^{1}H measurement, the existence of fewer, well-separated ^{13}C lines in a typical ^{13}C spectrum of a reaction mixture might make such measurements possible (see Section IV.D).

4. *Coke Deposition*

A natural extension of the studies of single pellet micro-imaging is to explore the effect of pore structure on the spatial distribution of coke deposition within the pellet. MR images have clearly shown that even while visual observations of pellets as a function of coking might be consistent with the shrinking-core model commonly employed in chemical engineering (i.e. coke deposition proceeds towards the centre of the pellet at a uniform rate such that the catalytically active region of the catalyst takes the form of a shrinking core of un-coked catalyst), coke deposition actually proceeds in a much more heterogeneous fashion with regions of coke deposition (of a length-scale corresponding to that of the length-scale of heterogeneities in the pore structure) occurring towards the interior of the pellet ahead of a higher concentration of coke deposition which is well described by the shrinking core concept (Cheah *et al.*, 1994). A more recent study by Bonardet *et al.* (1999) employs a different strategy. These workers imaged the ^{1}H spin density associated with 2,3-dimethylpentane adsorbed on pellets of HY zeolites coked to levels of 7.5 and 10% (w/w). The 1-D image profiles of the 7.5% (w/w) coked sample showed a heterogeneous coke distribution in the pellet at the macroscopic level. The most heavily coked region is that which was first exposed to reaction, and the heterogeneity in coking was again found to be associated with structural heterogeneities arising from the pellet manufacturing process. Bonardet *et al.* also concluded that the coke is heterogeneous in quality throughout the pellet. By varying the echo time in the r.f. pulse sequence it was found that the T_2 of the probe molecule, which is a function of the aromaticity of the coke, varies within the pellet. In particular, the more heavily coked zones were associated with coke characterised by the shortest T_2 values, indicative of coke of the most graphitic content. The more highly coked sample had a more homogeneous coke distribution, with the coke being of a homogeneous graphitic content throughout. A third approach to addressing coke deposition has recently been demonstrated by Bar *et al.* (2002), in a study of the location of coke deposits in industrial HZSM-5 pellets, of diameter 5 mm, contained in a small fixed-bed reactor. The coke distribution

was detected directly using the Single Point Ramped Imaging with T_1 Enhancement (SPRITE) technique, a special MR imaging sequence for detecting materials with short T_2 relaxation times. In the example given, SPRITE was used to produce a 1-D coke profile along the axis of the model fixed bed of inner diameter 3 cm, containing two layers of coked pellets (20.5 wt% coke) separated by a 3.3-cm layer of fresh pellets. A spatial resolution of 0.5 cm was obtained, this being limited by the rapid nuclear spin relaxation times of the sample. These workers also used an approach similar to that of Bonardet *et al.* (1999), in which the presence of carbonaceous deposits is observed indirectly by imaging the ^{1}H spin density of propane loaded within the sample. The different adsorption strengths of propane on the fresh and coked HZSM-5 cause T_4 to vary between the fresh and coked regions, hence allowing the regions of coked and fresh catalyst to be identified. The effect of coke deposition upon pore structure and molecular diffusion within supported-metal catalysts has also been studied (Wood and Gladden, 2003).

C. Single-Phase Flow in Fixed-Bed Reactors

There exist a wealth of studies of spatially unresolved measurements of single-phase flow in model porous structures such as bead packs (e.g. Manz *et al.*, 1999a; Seymour and Callaghan, 1997; Stapf *et al.*, 1998). The motivation for many such studies has been to understand flow within the porous structure of rock cores. In particular, PGSE-MR techniques have been used to measure diffusion and dispersion within such systems. However, it was not until relatively recently that the relevance of these measurements to the study of flow in fixed-bed reactors was identified. Indeed, fixed beds of column-to-particle diameter ratio 10–20 are an ideal system in which to apply MR flow imaging experiments since the flow field within the inter-particle space can be well resolved. While many industrial reactors are characterised by column-to-particle diameter ratios >20, the results obtained for these narrower beds are still relevant. Importantly we have shown that the major feature of the flow field observed in narrow beds (i.e. channelling throughout the entire bed, not just at the walls) is still observed for beds of column-to-particle diameter ratio of $\sim$40 (which is the largest bed we have studied). It should also be remembered that studies of beds of column-to-particle diameter ratio $\leqslant 20$ will be directly relevant to reactor designs used for reactions characterised by high exothermicity and relatively poor heat transfer, such as the synthesis of methyl-isobutyl ketone (Mariani *et al.*, 2001) and the conversion of natural gas into transportation fuels (Sie *et al.*, 1991). Even when the ultimate objective is in understanding the operation of larger column-to-particle diameter ratio beds, the MR imaging data are still valuable since they provide a wealth of data that can be used for the development and validation of numerical codes, which can then be used in subsequent scale-up studies. Further, MR imaging may also be used to identify

a specific phenomenon that influences process operation; once identified it may then be possible to develop a cheap, robust probe, such as pressure drop measurement, to monitor that phenomenon at plant-scale.

Early MR flow imaging studies of single-phase flow in fixed beds were reported for packings of non-porous particles. Figure 25 shows 2-D sections through 3-D volume images of the x, y and z components of flow within a fixed bed of non-porous spherical particles. The map of the z-component of the flow velocity is the most interesting; the $+z$-direction is the direction of superficial flow in the reactor. In this particular example, the superficial flow velocity was 0.56 mm/s, corresponding to a Reynolds number of 2.8. Hence, flow in much of the bed is dominated by viscous forces, associated with flow velocities less than, or of the order of, the superficial velocity. The most striking characteristic of these images is the extent of heterogeneity in the flow field; a relatively small fraction of the inter-particle space carries a high percentage of the liquid flow (Sederman *et al.*, 1997, 1998). Such regions of the bed are associated with high fluid velocities, and inertial effects increasingly influence the flow profile (Johns *et al.*, 2000). On the basis of these images, it is clear that any theoretical analysis of the flow within such a reactor must account for distinct populations of fast- and slow-moving liquid, as channelling does not just occur at the walls of the bed. The contact time between feed and catalyst will differ very significantly

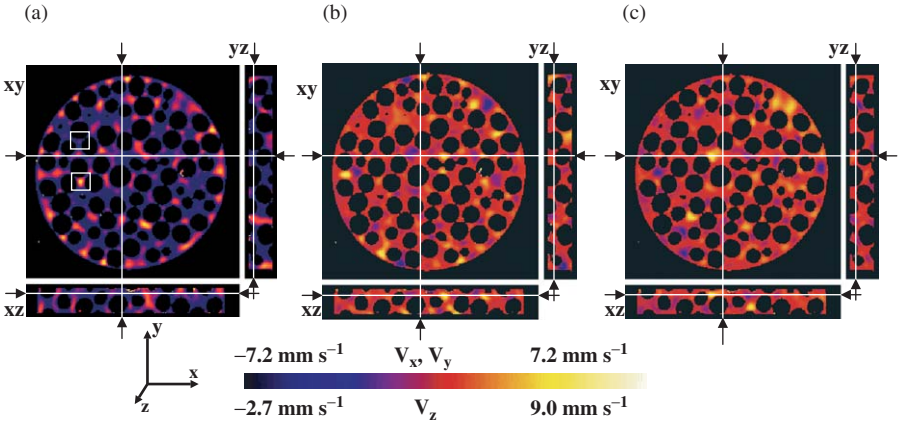

FIG. 25. MR visualisation of water flowing within a fixed bed of spherical glass beads; the beads have no MR signal intensity associated with them and are identified as black voxels. Flow velocities in the (a) z- (b) x- and (c) y-directions are shown with slices taken in the xy, yz and xz planes for each of the velocity components. For each image the positions at which the slices in the other two directions have been taken are identified. Voxel resolution is 195 μm × 195 μm × 195 μm. The glass beads are of diameter 5 mm and are packed within a column of internal diameter 46 mm. Typically 40% of the flow is carried by ~20% of the inter-particle space within any 2-D slice section through the bed, perpendicular to the direction of superficial flow. Regions of high and low flow velocity in the direction of superficial flow are highlighted in (a). Reprinted from Sederman and Gladden, (2001a), with permission from Elsevier. Copyright (2001).

across the bed, i.e. by up to at least one order of magnitude in regions of the bed characterised by the highest and lowest flow velocities, and this will introduce spatially varying mass transfer characteristics within the bed. The spatial resolution of the flow field is such that the flow profile between individual particles can be extracted from the data. This is clearly illustrated in Fig. 26 in which it is seen that at low velocities (or more precisely, at low local Reynolds numbers) parabolic, laminar flow is observed, whereas at higher local velocities the flow profile flattens such that it is much more characteristic of plug flow. MR data of this type are useful for identifying how catalyst size, shape and method of loading into the reactor influence heterogeneities in hydrodynamics while, at a more academic level, the combination of 3-D MR images of the bed structure with flow visualisation allows us to explore how the geometry and interconnectivity of the inter-particle space determine the local flow characteristics within the bed. These insights increase our generic understanding of fluid transport in porous materials and are equally relevant to understanding fluid transport processes in rocks and soils, with immediate application to oil recovery and groundwater remediation processes, respectively.

Figures 27 and 28 show how the combined application of MR imaging and flow visualisation allows us to study the deposition of fines within fixed beds. This is a common problem in reaction engineering. For example, during process

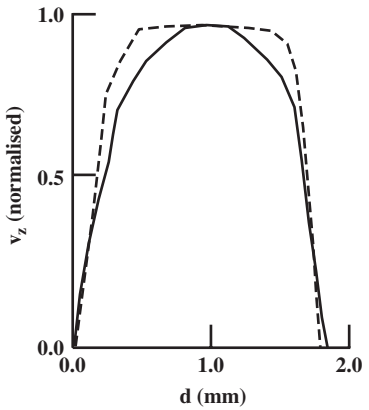

FIG. 26. The velocity profile for flow of water through two different regions (highlighted in Fig. 25a) of the inter-particle space within a fixed bed of spherical glass beads. The velocity profiles are measured across the inter-particle space between two packing elements. Profiles are shown for local regions associated with fast and slow flow velocities, characterised by a local Reynolds number of 50 and 12, respectively. At low *Re* number, a parabolic flow profile typical of Poiseuille flow is seen (——). At the higher *Re* number, inertial effects in the flow are evident and the flow profile approaches that of plug flow (——). For this particular bed, the *Re* number based on bed diameter is 15. Designs based on such a value of *Re* may well not adequately describe the true hydrodynamics of the system. *Re* is defined as $\left(\rho v A^{1/2}/\mu\right)$ where ρ and μ are the density and viscosity of the fluid phase, and v and $A^{1/2}$ are a characteristic fluid velocity and length-scale, respectively, of the system under study. Reproduced with permission from Johns *et al.* (2000). Copyright (2000), A.I.Ch.E.

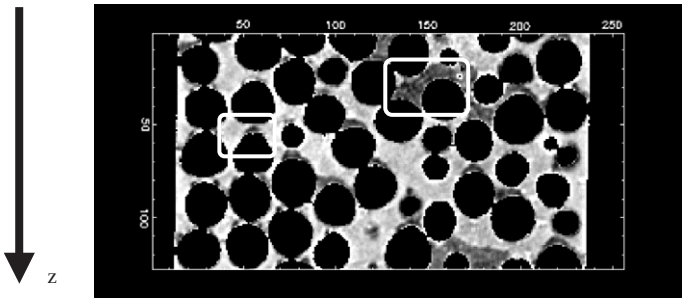

FIG. 27. 2-D-MR image of the deposition of 80 μm particles ("fines") within a bed packed with 5 mm spherical glass beads. The water flowrate was 300 ml/min. All images were acquired in 3-D with isotropic spatial resolution of 188 μm × 188 μm × 188 μm. Two local regions associated with a build-up of fines are highlighted, and are identified by the low apparent ^{1}H spin density from these regions resulting from low voidage and relaxation time effects. Flow is in the $+z$-direction. Reprinted from Gladden (2003), with kind permission of Springer Science and Business Media.

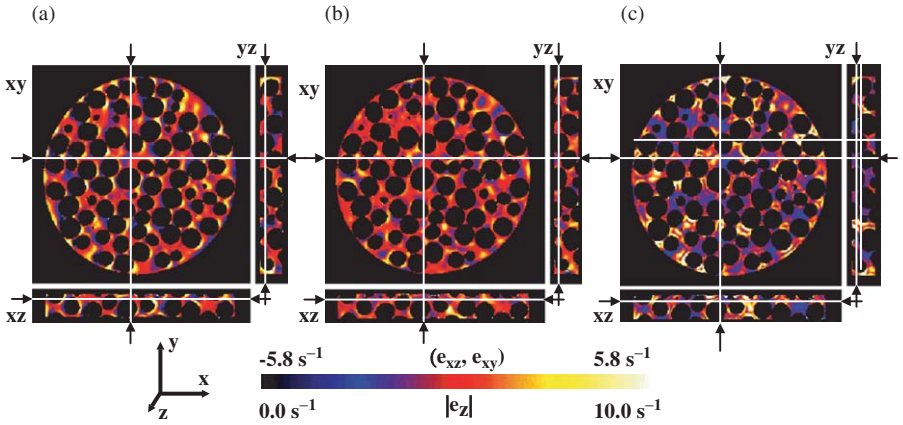

FIG. 28. Images of the liquid stress tensor derived from the data shown in Fig. 25. Data are shown for (a) e_{xz}, (b) e_{xy} and (c) $|e_z|$ with slices taken in the xy, yz and xz planes for each of the shear components. Regions of high shear are particularly evident in (c), i.e. along the direction of superficial flow, z. Reprinted from Sederman and Gladden (2001a), with permission from Elsevier. Copyright (2001).

operation, attrition of the catalyst will occur, and the resulting "fines" will deposit throughout the bed. These deposits will then influence the flow paths through the bed and this, in turn, can influence the operating conditions within the bed (e.g. pressure drop) and chemical conversion. Exactly the same experimental strategy would allow us to understand and optimise filtration processes. Figure 27 shows an image of water concentration (or, more precisely, ^{1}H spin density) within a 2-D slice section through a fixed bed of glass beads. The beads

are seen as black on the colour scale and the free water as white. Regions in which fines are deposited are readily identified as the grey contrast level; when fines are deposited, they pack to produce regions of low voidage, and are hence observed as regions of reduced water (^{1}H) content. The images shown in Fig. 28 explain how the MR flow images shown in Fig. 25 may be used to understand the phenomena leading to deposition. Figure 28 shows maps of the shear stress in the liquid as it moves through the bed. These maps of shear stress within the fluid have been calculated directly from the flow visualisations shown in Fig. 25 (Sederman and Gladden, 2001a). From these maps, we see precisely where regions of high liquid shear stress (lighter shades) exist within the bed; such regions will be associated with particle erosion but are not likely to be regions in which significant fines deposition will occur. In contrast, in regions of low shear stress little particle erosion will occur, but we will expect these regions to be particularly susceptible to fines deposition. As regions of particle deposition extend within the bed, the hydrodynamics and pressure drop characteristics of the bed will also change. Such images can be used directly in optimising the hydrodynamic characteristics of the bed to promote or minimise the existence of particular flow phenomena.

High-resolution images of the type shown in Fig. 25 combined with 3-D high-resolution images of the structure of the bed can also be used to study the more fundamental aspects of structure–transport relationships characterising the fixed bed itself. In a series of papers (Baldwin *et al.*, 1996; Johns *et al.*, 2000; Sederman *et al.*, 1997; Sederman *et al.*, 2001) it has been shown that in addition to extracting data such as radial distribution functions of either the void space or packing elements, image-analysis techniques can be used to partition the void space characterising the bed into individual elements—referred to as ''pores''—which are characterised by their volume, surface area and connectivity to each other. By combining this information with the images of flow occurring within the same bed, the influence of pore size, shape and connectivity on the flow within the void space of the bed can be investigated. This field is now receiving increasing interest both at an academic level and also from catalyst manufacturers interested in investigating how subtle changes in pellet size and shape can influence the spatial distribution of porosity and, hence, the hydrodynamics within the reactor (e.g. Gotz *et al.*, 2002). As in the case of the micro-imaging studies mentioned earlier (Section IV.B), a real advantage of employing MR techniques is the ability to quantify the extent and nature of heterogeneity in both structure and transport characteristics characterising the system under study.

The combination of techniques and research methodology described above is being applied to other fields. Examples include assessing the performance of filtration processes (e.g. Dirckx *et al.*, 2000) and biofilm reactors (e.g. Beuling *et al.*, 1998; Nott *et al.*, 2001). Both these applications exploit the capability of measuring the flow field within the process unit in combination with imaging the internal structure of the system so as to understand the inter-relationship of the

rate of formation and structure of deposited material with the local and macro-scale hydrodynamics. Other applications include visualisation of flow within hollow-fibre bioreactors (Heath *et al.*, 1990), and heat exchangers (Pangrle *et al.*, 1992; Sun and Hall, 2001; Wang *et al.*, 1999). Extensive studies of chromatographic column design and operation have been published by Tallarek, Van As and co-workers addressing issues such as the quantification of the mass transfer between the intra-particle pore network of the porous particles and the inter-particle void space comprising the column, as well as dispersion and electroosmotic perfusion phenomena (Tallerek *et al.*, 1996, 1999, 2001).

D. Measuring Chemical Composition and Mass Transfer in Fixed-Bed Reactors: In Situ Studies of Reactions

Recently, there has been a surge of interest in this area, but it is important to remember that early studies were reported as far back as 1978, albeit in relatively simple systems. In 1978, Heink *et al.* (1978) used 1-D profiling to study the time-resolved concentration profile of butane and water in packings of NaCaA and NaX crystallites, respectively. Other early studies include the use of ^{19}F imaging to follow the intercalation of AsF_5 into highly oriented pyrolytic graphite at room temperature (Chingas *et al.*, 1986). Since then, interest has focussed mainly on oscillations and travelling waves during chemical reaction (Balcom *et al.*, 1992; Menzinger *et al.*, 1992; Ra'bai *et al.*, 1990; Scott, 1987; Tzalmona *et al.*, 1990, 1992). Butler *et al.* (1992) employed ^{1}H-MR imaging techniques to investigate the extent of reaction in a single crystal of 4-bromobenzoic acid during exposure to ammonia gas. A second case study used MR imaging to follow the reaction of a deep bed of powdered toluic powder with ammonia gas flowing over it. The apparent reaction rate constant and the effective ammonia diffusion coefficient (into the toluic bed, perpendicular to the direction of flow) were obtained from a fit of a diffusion–reaction model to the experimental data. In principle, all the methods of MR spectroscopy can be integrated into an MR imaging sequence; hence, spatially resolved measurements of chemical conversion should be possible. However, the practical challenges in achieving this are substantial. In particular, as with any measurement, achieving adequate signal-to-noise is the key to a successful measurement. This is why in the vast majority of MR imaging experiments, signal from the ^{1}H nucleus is acquired. The ^{1}H nucleus has high MR sensitivity and exists in 100% natural abundance. The problem is that in any reaction mixture there is likely to be a wealth of ^{1}H resonances many of which will overlap, making it impossible to follow the change in concentration of a particular species. This problem is increased because of the interaction of the fluid phase with the solid-phase catalyst pellets, which causes the relaxation times of the fluid species to decrease. This further reduces the available signal-to-noise in the experiment and also broadens the spectral resonances, further increasing the overlap of individual

resonances. For this reason ^{1}H studies are likely to be limited to the study of simple reactions in which the ^{1}H spectral peaks are readily resolved. Alternatively, we must also consider ^{13}C, ^{31}P and ^{19}F imaging, if possible. ^{31}P and ^{19}F are commonly used in the medical field and have high abundance and sensitivity. ^{13}C is the most likely candidate species to be studied in heterogeneous catalytic processes, but successful implementation of the technique is not straightforward. Despite these difficulties, initial ^{1}H experiments and, most recently, the first report of ^{13}C observation in this application suggest that substantial new insights into the coupling of hydrodynamics and chemical conversion can be obtained by developing the appropriate MR techniques.

Albeit in a simple reaction, the nature of the information that can be obtained regarding chemical mapping and quantification of mass transfer processes has been demonstrated using the liquid-phase esterification of methanol and acetic acid catalysed within a fixed bed of H^{+}-ion exchange resin (particle size 600–850 μm). The purpose of this initial experiment was to confirm the link between the heterogeneity in hydrodynamics identified in Section IV.C and possible heterogeneity in conversion within the bed. This study is a good example of how the attributes of MR spectroscopy and imaging can be combined. In principle, there is no reason why the chemical mapping of the experiment cannot be performed at the spatial resolution achieved in the imaging of the structure of the bed. However, in the present example, spectra were acquired from relatively large volumes within the bed (1.5 mm × 1.5 mm × 0.5 mm) to ensure high signal-to-noise data for subsequent analysis. Using this approach, we were able to study quantitatively the extent of conversion at various locations within transverse sections through the bed and at several positions along the length of the bed. The experiment is reported in detail elsewhere (Yuen *et al.*, 2002). The technique of volume-selective spectroscopy (Kimmich and Hoepfel, 1987) is used to obtain, non-invasively, MR spectra from the well-defined volume elements with the bed; this is achieved by the application of magnetic field gradients to selectively excite spins only within the volume of interest. The chemical conversion within each volume is obtained directly from the positions of the spectral peaks within the ^{1}H spectrum. The measurement of chemical composition, and hence conversion, within the bed is entirely non-invasive, thereby overcoming the problem of introducing sampling points within the bed, which will disturb the local hydrodynamics and potentially influence the local conversion. It is worth summarizing the principle of the measurement since it is a way of overcoming the problem of not being able to resolve molecule-specific resonances (or 'peaks') in the ^{1}H spectrum. Quantification of chemical composition is achieved by exploiting the phenomenon of fast exchange of the ^{1}H species associated with hydroxyl groups within the acetic acid, methanol and water species comprising the reaction mixture:

$$CH_3OH + CH_3COOH \rightleftharpoons CH_3COOCH_3 + H_2O \tag{23}$$

As a result of ^{1}H fast exchange, the observed chemical shift (i.e. resonance frequency) for the ^{1}H species associated with OH groups present in the reaction mixture ($\delta_{observed}$) is determined by an average of the component chemical shifts, weighted by the amount of each molecular species present, as follows from Eq. (23). Thus, the concentration of acetic acid present at any time and, hence, the extent of conversion at that time is determined directly from the value of $\delta_{observed}$ identified in the volume selective spectrum. Figure 29 shows a 2-D slice section through a 3-D RARE image of the bed; the image voxels are of size $97.7\,\mu m \times 97.7\,\mu m \times 97.7\,\mu m$. ^{1}H-MR spectra have been recorded from regions of in-plane dimension $1.5\,mm \times 1.5\,mm$, with a slice thickness of $500\,\mu m$ in the direction of superficial flow. From each spectrum it is possible to determine, directly and quantitatively, the extent of conversion within a given local volume, as shown in Figure 30. All images in Fig. 30 show that there is significant heterogeneity in conversion within a single transverse section through the bed, perpendicular to the direction of superficial flow; fractional variations in conversion of up to ~20% are typical under steady-state operating conditions. Although such studies are in their early stages, we clearly have the measurement tools to study the complex interaction of hydrodynamics and chemical kinetics in the complex porous medium represented by a fixed bed.

While the esterification experiment described in the previous paragraph has provided the most detailed *in situ* visualisation of a heterogeneous catalytic reaction to date, the approach to measuring conversion cannot be used routinely for other reactions. This is because we are monitoring quite small variations in chemical shift to calculate conversion, which requires a relatively simple ^{1}H spectrum that can be interpreted unambiguously. Two other studies have been reported recently. In the first of these, Koptyug *et al.* (2004) used ^{1}H-NMR to produce spatially resolved spectra within a 2-D slice section along the axial direction of a fixed bed of Pd/Al_2O_3 (1%, (w/w)) catalyst pellets. The reaction considered was that of the hydrogenation of α-methylstyrene to cumene. The spectra show clear evidence of changes in chemical composition along the length of the bed, but conversion is not quantified, most likely owing to problems in deconvolving the ^{1}H resonances from the reactant and product species. The most recent study reports the successful implementation of ^{13}C imaging to study reaction *in situ* (Akpa *et al.*, 2005), illustrated by the competitive etherification and hydration reactions of 2-methyl-2-butene occurring within a fixed bed of H^{+}-ion exchange resin. By exploiting polarisation transfer techniques, sufficient signal-to-noise is achieved for spatial resolution of chemical composition, and hence conversion, within the bed to be obtained without the need for ^{13}C isotopic enrichment. Although much work remains to be done, the ability to spatially map ^{13}C signals at natural isotopic abundance opens up significant new opportunities for widespread studies exploring the interaction of hydrodynamics, mass transfer and chemical kinetics within catalytic reactors. Our ultimate goal must be to gain enough understanding to design an integrated, optimised (scaled-up) catalyst reactor system that can deliver the

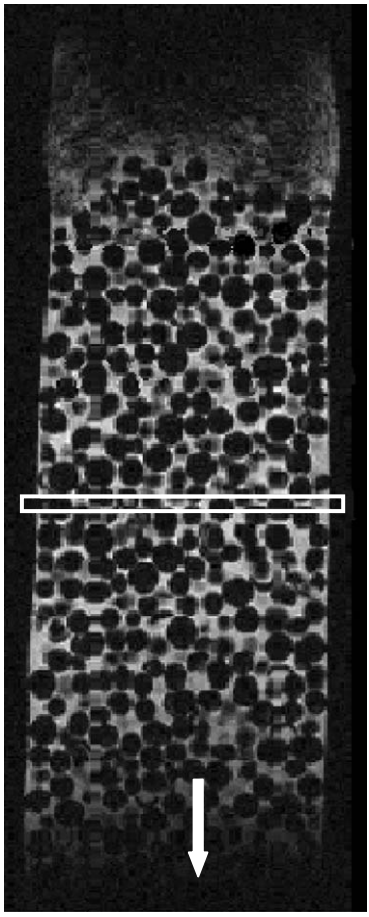

FIG. 29. 2-D slice through a 3-D RARE image of a fixed bed of ion exchange resin. The image has an isotropic resolution of 97.7 μm × 97.7 μm × 97.7 μm. The image slice in which the local volumes are located for the volume-selective spectroscopy study is identified. The image was acquired by saturating the bed with pure methanol. The image is acquired employing T_2 contrast such that signal is acquired only from the methanol in the inter-particle space. The arrow indicates the direction of superficial flow. Reprinted from Gladden (2003) with kind permission of Springer Science and Business Media.

high activities and selectivities that the catalyst can achieve at small scale in powder form.

Further extensions of chemical mapping within a fixed bed lie in quantifying mass transfer between the intra-pellet and inter-pellet pore space. One approach to measuring mass transfer processes is to use displacement propagator measurements (see Section II.C). The data acquired for the esterification reaction described previously are shown in Fig. 31. In this propagator measurement, the total propagator measured for the system has been separated into two

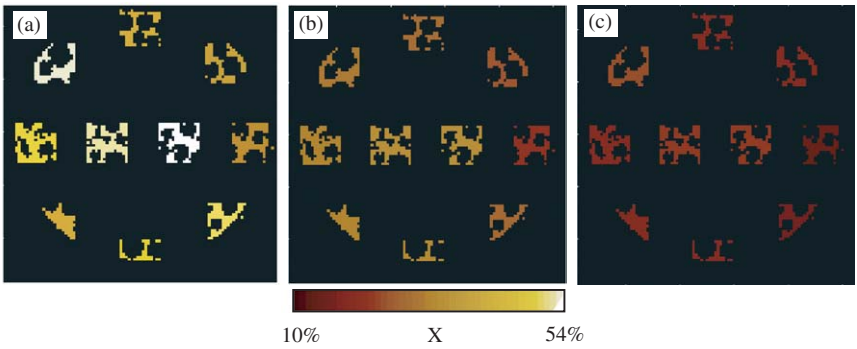

FIG. 30. Visualisation of mean conversion, X, within selected volumes located within the slice section identified in Fig. 29. The local volumes have in-plane dimensions of 1.5 mm × 1.5 mm, and have a depth (image slice thickness) of 500 μm. Data are shown for three feed flow rates: (a) 0.025, (b) 0.05 and (c) 0.1 ml/min. As flow rate increases, so the residence time characterising the bed decreases and it therefore follows that conversion will decrease. Reprinted from Gladden (2003), with kind permission of Springer Science and Business Media.

component propagators by combining the transport measurement pulse sequence with a spin-lattice relaxation time experiment. Since the relaxation time of liquid molecules that have existed only within the inter-particle space during the observation time (100 ms) of the experiment is significantly longer than that of molecules that have moved between the inter- and intra-particle space, independent propagators characterising these two populations of liquid molecules can be obtained (Gladden *et al.*, 2003a). In Fig. 31 the broader propagator, which shows two peaks, is that associated with the liquid in the inter-particle space. The two peaks are consistent with there being populations of very slow-moving and much faster moving fluid within the bed—note that these observations confirm that the flow heterogeneity observed in beds of low column-to-particle diameter (~10—Fig. 25) is also observed for beds of significantly higher column-to-particle ratios (~20). The full-width at half maximum of the (narrower) "exchange" propagator provides an estimate of the effective diffusion coefficient for water molecules moving between the pore space of the catalyst and the inter-particle space of the bed of $\sim 2 \times 10^{-9}\,m^2/s$, which gives a lower limit to the value for the mass transfer coefficient of $\sim 4 \times 10^{-6}\,m/s$. This value is obtained by defining a mass transfer coefficient as D/δ, where δ is a typical distance travelled to the surface of the catalyst that we estimate as half a typical bead dimension (~500 μm). Such a mass transfer coefficient would give rise to a rate of reaction of $\sim 2 \times 10^{-3} s^{-1}$, consistent with the reaction occurring under conditions of kinetic control.

E. Two-Phase Flow in Fixed-Bed Reactors

The next level of complexity in implementing MR to study fixed-bed processes is to study two-phase flow phenomena. Initial studies focussed less on fully

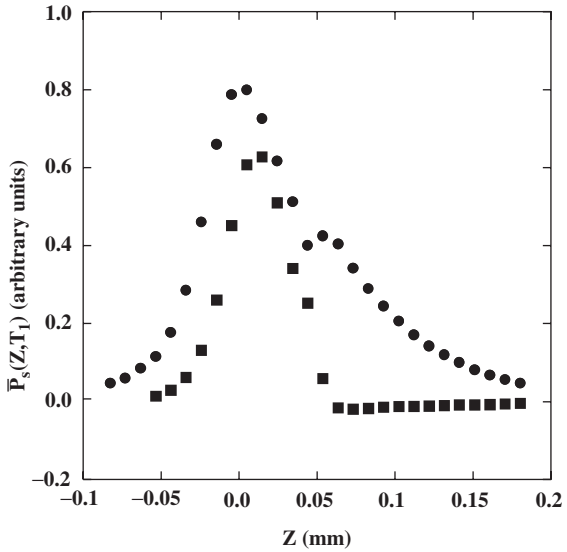

FIG. 31. T_1-resolved propagators for water flowing within the inter-particle space of a bed packed with ion exchange resin (●) and for water exchanging between inter- and intra- particle environments (■) during the timescale of the transport measurement. Data are shown for a volumetric feed flow rate of 2 ml/min, to a column of internal diameter 20 mm.

resolving the liquid flow field and more on the macroscopic gas–liquid distribution within the bed, with the specific aim of measuring liquid holdup (χ) and surface wetting. The latter is particularly important since MR provides the first, direct, non-invasive measure of this quantity. The first reported MR imaging study of liquid holdup and wetting in two-phase flow within a fixed bed was performed on a column of internal diameter 40 mm, packed with 5-mm-diameter non-porous glass spheres (Sederman and Gladden, 2001b). This system was considered a model system for a trickle bed, and it was demonstrated that measurements of both liquid holdup in quantitative agreement with gravimetric data, and surface wetting could be obtained directly. The typical spatial resolution obtained in these measurements was ~300 μm; therefore, the absolute thickness of wetted films on the surface of the packing elements is not imaged. Instead, by selecting a suitable gating level on the image intensity that discriminates between image pixels that are part-filled with liquid (i.e. containing a solid/gas/liquid interface) and those that have zero liquid content, it is possible to identify the presence of liquid films on the surfaces of the glass spheres unambiguously. Liquid holdup and wetting efficiency (χ_s), as defined below, were determined:

χ.—The fraction of (inter-particle) void space pixels containing some liquid provides an upper estimate of liquid saturation, from which values of liquid holdup are obtained. By extrapolation of the data to zero liquid superficial

velocity, the static liquid holdup is identified, and the dynamic liquid holdup, $\chi_{dynamic}$, is obtained.

χ_s.—The wetting efficiency is obtained by calculating the fraction of the pixels identifying the surface of the packing that are in contact with liquid during gas–liquid flow. Liquid-containing voxels adjacent to the wall of the column, and the internal surface of the porous packing elements are not considered in the analysis.

Figure 32 shows the nature of the data obtained. In Fig. 32b the total liquid holdup in the image slice has been segmented in to what we call rivulets using the pore space segmentation algorithm referred to in Section IV.C. Application of this algorithm is merely an objective, reproducible procedure to characterise the liquid distribution within the bed. By recording these data in 3-D, a range of statistics can be produced, such as the number of "pores" within the bed associated with different levels of fractional filling and the number distribution of the fractional surface wetting of the packing elements.

Extension of this methodology to packings of porous packing elements (e.g. catalyst support pellets) is not straightforward. The challenge arises because the signal we wish to measure is associated with the water in the bed. However, the signal intensity we acquire from a specific region of water will depend on its local environment, because the nuclear spin relaxation times of water in different physical environments will be different. In this system, the different environments will be (i) free water in the bulk of the inter-pellet space, (ii) water

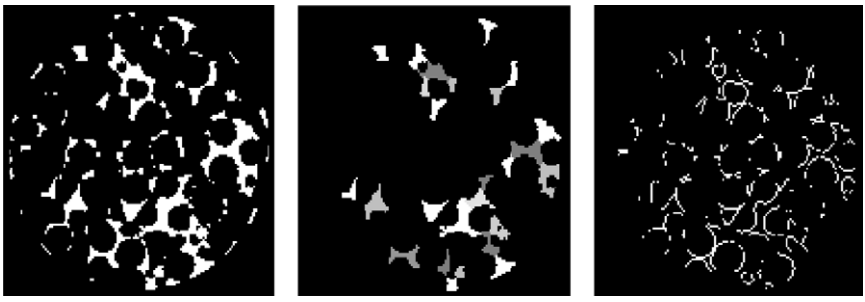

FIG. 32. Identification of rivulets and surface wetting in a packing of 5 mm diameter glass spheres contained within a column of internal diameter 40 mm. The data were acquired in a 3-D array with an isotropic voxel resolution of 328 μm × 328 μm × 328 μm. (a) The original image of trickle flow was first binary-gated, so that only the liquid distribution within the image is seen (white); gas-filled pixels and pixels containing glass spheres show up as zero intensity (black). (b) The liquid distribution is broken up into individual liquid rivulets, each identified by a different shade on a grey scale. (c) Pixels containing any liquid–solid interface are then identified using image analysis techniques and "images" of surface wetting are produced. Data are shown for liquid and gas superficial flow velocities of 3 and 66 mm/s, respectively. Reprinted from Sederman and Gladden (2001b), with permission from Elsevier. Copyright (2001).

within the intra-pellet pore space and (iii) water existing in films on the surface of the pellets but not part of a rivulet within the inter-pellet space. Initial studies of holdup and wetting during trickle flow in a fixed bed packed with cylindrical, porous alumina extrudate have been reported. Data were presented for two packings: (i) packing of diameter 1.5 mm and a distribution of lengths in the range 5 ± 2 mm; (ii) packing of diameter and length equal to 3 mm. A constant gas superficial velocity of 31.3 mm/s was used, with liquid superficial velocities in the range 0.1–6 mm/s. 2-D visualisations of liquid distribution within transverse sections, of thickness 1 mm, were acquired. The total data acquisition time for each image was 25 min. Data were recorded with a field-of-view of 40 mm × 40 mm and a data array size of 256 × 256, thereby yielding an in-plane spatial resolution of 156 μm × 156 μm (Gladden *et al.*, 2003b).

Figure 33 shows plots of dynamic liquid holdup and wetting efficiency against liquid superficial velocity for a constant gas velocity of 31.3 mm/s (Gladden *et al.*, 2003b). It is clearly seen that dynamic liquid holdup increases more rapidly as a function of liquid superficial velocity within the 1.5 mm packing, and values of holdup and wetting efficiency are always greater, for a given liquid velocity, for the 1.5-mm-diameter packing relative to the 3-mm-diameter packing. The line through the dynamic liquid holdup data is the best fit of the percolation-based model described by Crine *et al.* (1992). The form of the expression for the dynamic liquid holdup is

$$\chi_{\text{dynamic}} = (KQ)^{1/3}\left(\frac{Q}{Q+Q_{\text{min}}}\right)^{2/3} \tag{24}$$

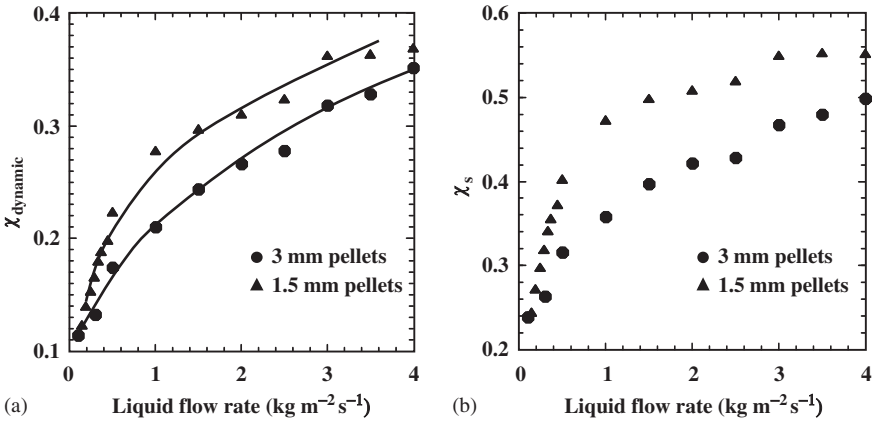

FIG. 33. (a) Dynamic liquid hold-up, and (b) wetting efficiency as a function of liquid superficial velocity for 1.5 and 3 mm cylinders. Gas flow rate is constant at 66 mm/s. The line shows the best fit of the percolation model of Crine *et al.* (1992). Reprinted from Gladden *et al.* (2003b), with permission from Elsevier. Copyright (2003).

where Q is the liquid superficial velocity and $Q_{\min}$ the minimum liquid superficial velocity. $K = k\mu_L a^2/\rho_L g$, where k is a proportionality factor depending on the fluid and packing properties, μ_L the liquid dynamic viscosity, ρ_L the liquid mass density, a the specific surface of the packing and g the acceleration due to gravity. Equation (24) is fitted to the experimental data, with $Q_{\min}$ and K (i.e. k) as variables in the fit. As seen from Fig. 33, the fit of Eq. (24) to the data is good. The values of $Q_{\min}$ obtained are 3.56×10^{-4} m/s and 12.5×10^{-4} m/s for the 1.5- and 3-mm-diameter cylinders, respectively. Following the argument of Toye *et al.* (1996), $Q_{\min}$ characterises solid-phase (i.e. packing) wettability such that smaller values of $Q_{\min}$ are associated with better packing wettability. This, as discussed earlier, is clearly supported by inspection of Fig. 33. These early studies of trickle flow within beds of porous packing elements identified three general results: (i) values of liquid holdup compare well, typically to within 5% of gravimetric data; (ii) the general trends in both holdup and wetting data are consistent with the predictions of existing models in the literature; (iii) the absolute value of surface wetting tended to be lower than that previously reported in the literature. Considering (iii), there are, of course, likely to be significant errors in the values of wetting obtained from the range of indirect methods used in the earlier works. However, an underestimation of surface wetting using data obtained from MR imaging can be explained as a consequence of not ''seeing'' liquid layers on the surface when they are not associated with a larger scale liquid rivulet. As a result of this observation, improved data-acquisition and image-analysis strategies have been developed. The key modification to the overall methodology is that we apply an image-analysis algorithm that applies a local gating level: this is an objective procedure that accounts for the fact that the gating level we choose must discriminate between intra-pellet water and water bound to the surface as a wetted film. The particular gating level needed to achieve this will be very sensitive to the signal from the intra-pellet water, and since this varies with the characteristics of individual pellets, a global gating level will always introduce inaccuracies into the measurement. Using this improved algorithm, MR measurements of both holdup and wetting are in good agreement with the predictions of the neural network analysis of Larachi *et al.* (1999).

F. Hydrodynamic Transitions in Fixed-Bed Reactors

Trickle- and pulse-flow regimes are the contacting patterns most commonly encountered in commercial-scale trickle beds; therefore, understanding the nature and characteristics of the hydrodynamics in these flow regimes and the transitions between them are subjects of long-standing interest (e.g. Blok *et al.*, 1983; Boelhouwer *et al.*, 2002; Dankworth *et al.*, 1990; Grosser *et al.*, 1988; Holub *et al.*, 1992; Larachi *et al.* 1999; Ng, 1986; Reinecke and Mewes, 1997; Sicardi and Hofmann, 1980). The flow pattern will significantly influence the performance of a given reactor through characteristics such as phase holdups,

power consumption and mass-transfer fluxes, so successful modelling of trickle-bed reactors requires precise tools for the identification of the flow pattern expected for a specified set of operation conditions. An accurate prediction of the trickle-to-pulse transition is also of key importance in this regard (Larachi *et al.*, 1999). Extending MR to study unsteady-state flows requires rapid data acquisition times. In this case, FLASH techniques (see Section II.F) were employed, and spatial resolution was reduced such that sufficient signal-to-noise was achieved. This is the subject of ongoing work, but some interesting new observations have already been made. This research also highlights that every time we implement a new type of data acquisition we have to think carefully about how to process the data so that the important information is captured. Images were acquired as a data array of size 32×16 (in-plane spatial resolution $1.4\,\text{mm} \times 2.8\,\text{mm}$), with an acquisition time of 20 ms for a 2-mm slice thickness. Images were acquired in immediate succession, and frame rates of 50 frames per second (f.p.s.) were achieved. The maximum number of images acquired in a single series was 540, this number being limited by hardware considerations. High-resolution images of 2-D slice sections through the bed were also acquired to provide accurate identification of the position of packing elements within the bed. These were acquired using a standard spin-echo imaging sequence with an in-plane resolution of $175\,\mu\text{m} \times 175\,\mu\text{m}$ for a slice thickness of 1 mm. The methods we have chosen are outlined below:

Signal intensity in the images is acquired only from the liquid phase. The MR imaging data obtained have been analysed using the following two procedures:

(i) *Standard deviation maps*: The simplest way to assess the stability of the gas–liquid distribution is to calculate a map of the standard deviation of the pixel intensities for each pixel in a time series of images. Thus, for a series of n images, the standard deviation of the intensity associated with pixel i, σ_i, is calculated as follows:

$$\sigma_i = \sqrt{\frac{\sum (x_i - \bar{x}_i)^2}{n}} \tag{25}$$

where x_i is the signal intensity of pixel i, and $\bar{x}_i$ the average intensity of pixel i in the series of n images, the summation being taken over n images.

(ii) *Temporal autocorrelation function* ($R_I(\tau)$) *plots of effective liquid holdup*: These are calculated from the signal intensity (i.e. effective liquid holdup) data as follows:

$$R_I(\tau) = \frac{\langle I(t) I(t+\tau) \rangle}{\langle I^2 \rangle} \tag{26}$$

where $I(t)$ is the total signal intensity within the region of interest acquired at time t. This analysis extracts correlations in the signal intensity for all time separations τ and highlights any periodicity in the holdup data and the timescales over which they exist.

Figure 34 shows three time series of 2-D magnetic resonance images of liquid distribution (Lim *et al.*, 2004). The three sets of operating conditions characterising these series correspond to operation in the trickle-, transition- and pulse-flow regimes. The gas velocity is constant at 112 mm/s, data in rows (a), (b) and (c) correspond to liquid velocities of 0.8, 6.8 and 10.6 mm/s, respectively. The final image in each series is the standard deviation map calculated from a series of 512 images acquired in immediate succession over a period of 10 s. It is clearly seen that the liquid distribution in each of the trickle-flow images (Fig. 34a) appears constant; therefore, the standard deviation map has pixel intensities approaching the noise level consistent with a given pixel containing the same phase or combination of phases (liquid, solid, gas) in each successive image.

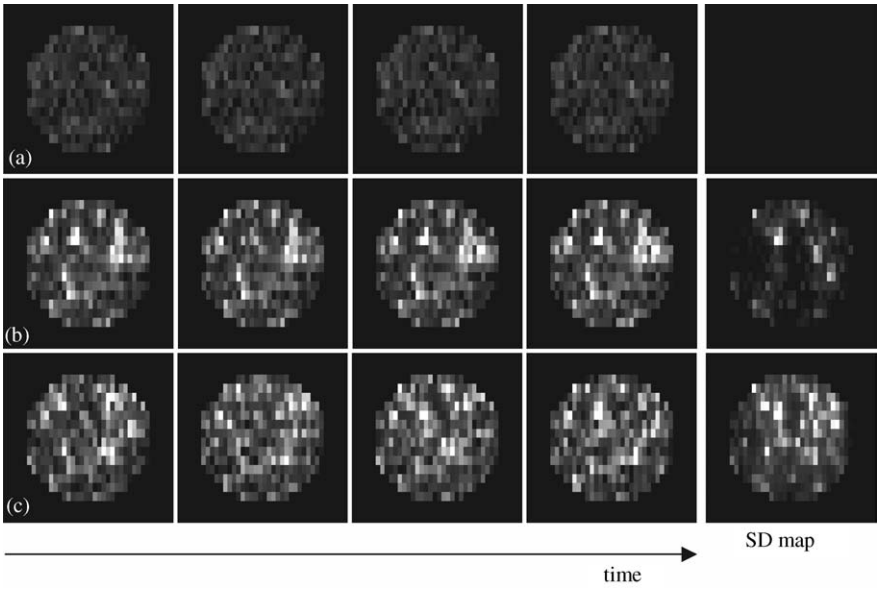

FIG. 34. Evolution of gas–liquid distribution in the (a) trickle-, (b) transition, and (c) pulsing-flow regimes. The gas velocity is 112 mm/s; liquid velocities are (a) 0.8, (b) 6.8 and (c) 10.6 mm/s. Four images are shown acquired within the series of 540; each image took 20 ms to acquire. High intensity (white) corresponds to high liquid content. Signal intensity is associated only with the liquid phase. In-plane spatial resolution is 1.4 mm × 2.8 mm, and the image slice thickness is 2 mm. All images are on the same intensity scale. The final image in each row is the SD map calculated from 512 consecutive images taken from the complete time-series acquired. The three standard deviation maps are plotted on the same scale with white (highest) and black (lowest) values. Reprinted from Lim *et al.* (2004), with permission from Elsevier. Copyright (2004).

Fig. 34c corresponds to conditions of pulsing flow during which the content (i.e. gas or liquid) of a given pixel changes with time. Thus, the resulting standard deviation map has high intensity values (lighter shades). There also exist regions within this standard deviation map that appear to suggest stable gas–liquid distribution. In many cases, such features in the standard deviation maps actually correspond to regions where the given image pixel contains (mostly) solid catalyst pellets. Since the pellets do not move, and remain liquid filled at all times, the signal intensity associated with that pixel, even if such a pellet is at times surrounded by either gas or liquid, will change very little. The series of images shown in Fig. 34b are taken for a set of conditions that exist at an operating condition within the transition from trickle to pulsing flow. Inspection of this row of images shows a constant gas–liquid distribution in most regions of the field of view. However, some regions clearly show a time-varying liquid distribution. The regions of stable and unstable liquid content are clearly identified in the associated standard deviation map and provide strong evidence in support of the "microscopic" models of the trickle-to-pulse transition. Movies of the 2-D images recorded in the trickle-, transition- and pulse-flow regimes can be found at the website http://www.cheng.cam.ac.uk/groups/mri/aichej.htm. Figure 35 explores the nature of these local pulsing events in more detail by overlaying the standard deviation maps with the high-resolution image of the structure of the bed; the pixels associated with pellets have been gated out and are depicted in black for clarity (Lim *et al.*, 2004). It is clearly seen that the initial local pulses occur at the size scale of the packing elements within the bed.

Further analysis of the standard deviation maps is extended by applying a binary gate to these data sets to identify pixels that are associated with values of standard deviation significantly above the noise level, thereby clearly identifying the position of local pulses within the bed. Figure 36a shows a binary-gated version of the standard deviation map shown in Fig. 34b. The value at which the binary gate is applied is chosen to be 5σ, where σ is the average standard deviation value of the noise calculated from the images of a completely liquid-filled bed. Figure 36b shows the temporal autocorrelation function data calculated from the two regions identified by the binary gate. The regions identified by black pixels, which identify pixels associated with a constant gas–liquid distribution, are characterised by a constant value of the temporal autocorrelation function of $\sim$1. The pixels associated with time-varying gas–liquid content are seen to have a temporal autocorrelation function containing several distinct periodicities. In Fig. 36c, local temporal autocorrelation functions are calculated for the local regions highlighted in Fig. 36a. Local periodicities of $\sim$0.4, $\sim$2 and $\sim$10 s are identified. The fluctuations in the liquid signal occurring with a period of $\sim$0.4 s are of much smaller magnitude. A possible explanation for this is that these fluctuations in liquid distribution are associated with fluctuating liquid films on the surface of the packing. This hypothesis is further investigated in Fig. 37, which shows the standard deviation map and temporal autocorrelation data for images recorded at a liquid and gas velocity of 2.0 and

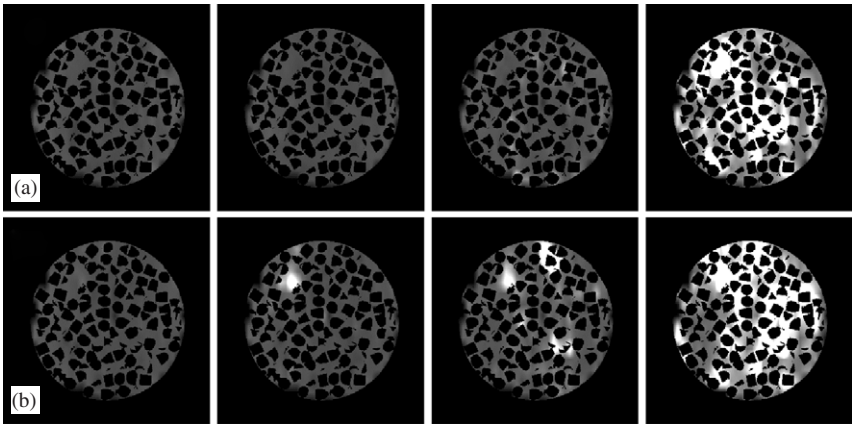

FIG. 35. Identification of location and size of local pulses within the trickle bed. A high spatial resolution image (in-plane spatial resolution 175 μm × 175 μm; slice thickness 1 mm) is overlayed with a standard deviation map calculated from images acquired at a spatial resolution of in-plane spatial resolution 1.4 mm × 2.8 mm, and slice thickness 2 mm. The standard deviation maps have been linearly interpolated to the same in-plane spatial resolution as the high resolution data. Images are shown for a constant gas velocity of 112 mm/s; (a) increasing liquid velocity, and (b) decreasing liquid velocity. The liquid velocities increase left to right: 2.8, 3.7, 6.1 and 7.6 mm/s. Reprinted from Lim *et al.* (2004), with permission from Elsevier. Copyright (2004).

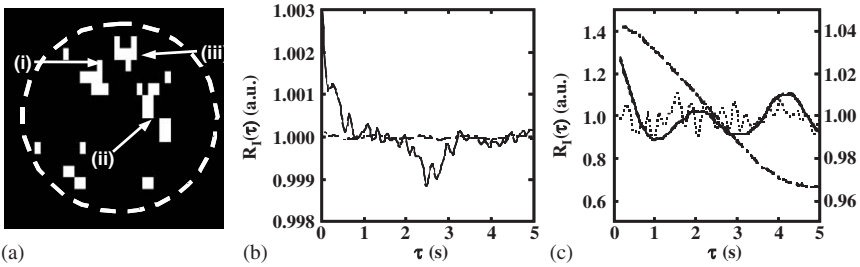

FIG. 36. (a) The binary-gated map derived from the SD map shown in Fig. 34b. The pixels identified as being associated with local pulsing are identified as white; pixels associated with "constant" gas–liquid distribution are identified as black. (b) The temporal autocorrelation function calculated for white pixels (——) and black pixels (- - - - -). (c) Local autocorrelation functions calculated from the identified regions (i, ii, iii) identified in (a) correspond to periods of oscillation of ~10, ~2 and ~0.4 s, respectively. The solid and dashed lines take the values on the left-hand *y*-axis; the much smaller scale intensity fluctuations are associated with the much smaller values of standard deviation on the right-hand *y*-axis. Reprinted from Lim *et al.* (2004), with permission from Elsevier. Copyright (2004).

275 mm/s, respectively. This condition lies in the trickle regime before the onset of the transition to pulsing flow. The standard deviation map is not shown on the same scale of intensity as those shown in Fig. 34. Instead, the scale varies between the highest (white) and lowest (black) values of standard deviation

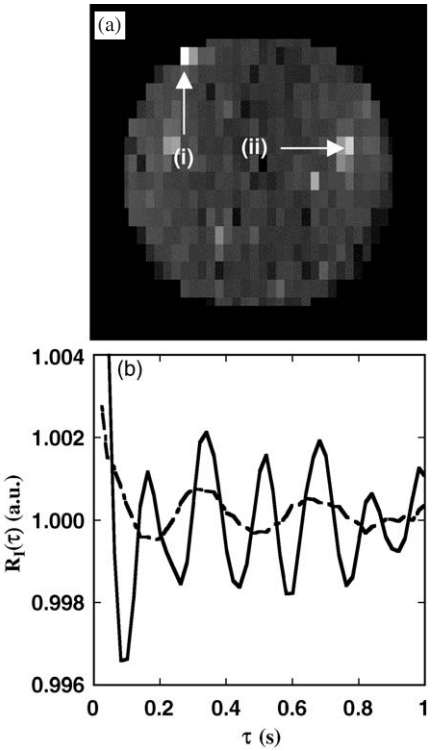

FIG. 37. (a) standard deviation map, and (b) temporal autocorrelation functions for data recorded at liquid and gas velocities of 2.0 and 275 mm/s, respectively. The grey scale varies between lowest (black) and highest (white) standard deviation values calculated. The temporal autocorrelation functions are shown for regions (i) and (ii) by solid and dashed lines, respectively. Reprinted from Lim *et al.* (2004), with permission from Elsevier. Copyright (2004).

calculated from this specific time series of liquid-distribution images. All the standard deviation values in Fig. 37a fall below the gating level selected for the data shown in Fig. 36a. Therefore, all the fluctuations in liquid distribution are much smaller than those observed when macroscopic (~size of the packing elements) liquid pulses occur. Short time-scale fluctuations in the local liquid distribution that occur with well-defined periods of ~0.15 and 0.3 s (see Fig. 37b) can be observed. This work has recently been extended to acquire 3-D images of the formation and evolution of local pulsing events through the trickle-to-pulse transition (Anadon *et al.*, in press; Gladden *et al.*, in press).

V. Future Prospects

The role of MR in chemical engineering research is changing. It is now established as a quantitative measurement tool in chemical engineering, and as its

use becomes more widespread the "language" of MR will appear less daunting. There remains significant scope to develop new MR methods that address specific measurement needs in chemical engineering. To this end we are likely to see continued interest in the development and implementation of fast measurement methods and increasing use of MR beyond ^{1}H to observation of nuclei such as ^{13}C, ^{31}P, ^{23}Na and ^{19}F. We are also likely to see MR systems dedicated to specific MR measurements set up for use by the non-expert. Precedents already exist in clinical medicine, downhole tools in oil exploration and food quality control. In each of these applications, MR hardware and software are designed to perform a restricted set of measurements such that the resulting data are readily interpreted in terms of specific characteristics of the system of interest. In addition to this simplified user interface, the design of hardware for a single specific function can also reduce hardware costs considerably. There is also potential for using dedicated, single-function MR hardware for process control applications. For example, droplet-size distributions in emulsions can be characterised *in situ* under flowing conditions, thereby enabling MR to be used as part of a process control strategy. This measurement technique also avoids the introduction of errors into the droplet-size determination caused by extracting samples from a process line for *ex situ* analysis (Johns and Gladden, 2002). Further opportunities lie in combining MR with other tomographic and sensor technologies. For example, X-ray micro-tomography (XMT) can probe structures at a higher spatial resolution than MR, but does not readily give information on transport processes. By combining MR and XMT, a greater range of spatio-temporal correlations may be accessed. Opportunities also exist in using MR to identify and understand, at the laboratory scale, the occurrence of particular phenomena that may have a detrimental effect on product quality or process performance, but then using a cheap, robust measurement on plant to identify when such phenomena occur in the real process. For example, in the context of trickle-bed operation, the detailed nature of transitions in hydrodynamics between different flow regimes may be determined and their signature in terms of variation in pressure drop measurements identified. The pressure drop measurements may then be used on the full-size operating unit to provide a much more accurate assessment of trickle-bed operation.

Having introduced and begun to validate the use of MR measurements, the integration of these measurements into numerical modelling and theoretical research will also be an area of significant opportunity and development. MR data can be used (i) to guide the description of the problem to be solved. This can be done by using the MR image directly, in pixelated form, as the simulation lattice, or by using the image in a more qualitative way to identify the structural features that need to be represented within the simulation, and (ii) to explore the accuracy of the numerical prediction. This is an area of research in which work in the medical and engineering fields is at a similar stage of development, which is not surprising since both research communities require each

other's skills. A good example of this research methodology is found in the work of Wang and Li (1998), which used MR images to develop a 3-D simulation lattice upon which a numerical simulation of the mass transport processes relevant to drug delivery to a brain tumour could be based. From this simulation it was possible to predict the optimal location of a controlled-release drug delivery implantation. One might ask, why is MR imaging so much more useful in this type of application compared with other tomographic techniques? Of course, the ability to image an optically opaque subject is key, but just as important is the fact that MR can also give a 3-D mapping of the transport processes occurring within the sample as well as mapping chemical composition—i.e. if one needs the real diffusion coefficients of species within the sample to input to the model, one can measure them directly. This is enormously powerful because we can develop models in which the simulation lattice, boundary conditions and many of the transport parameters required by such models are not free variables but parameters measured on the real system.

More generally, the ability of MR to provide 3-D data sets for the validation and development of numerical codes (e.g. Manz *et al.*, 1999c) will be enormously useful. As we look to the future, many of us expect that we will be able to exploit developments made in computational physics so as to provide an alternative strategy to using scale-up rules and correlations in process design. If this goal is to be achieved, these "predictive" codes must be validated rigorously, and MR has an important role to play in this. The key attribute of MR is its ability to provide spatially resolved information on structure, transport and, as appropriate, chemistry, within the system of interest. If the numerical code is able to predict, at high spatial resolution, the experimentally determined chemical composition, diffusion, dispersion and flow behaviour then there is compelling evidence that the code is capturing the correct chemistry and physics, and hence should be able to predict the performance of the scaled-up system. Of course, strategies will still be required for modelling heterogeneities in macro-scale systems on length-scales greater than those probed in the MR experiments.

In conclusion, this chapter has attempted to bring together the measurement capabilities that can be united under the heading of "MR techniques". Each of these can be a research field in their own right, but from the perspective of the chemical engineer it is the combination of these methods—particularly in the hierarchy of length-scales they probe—that makes MR methods so powerful.

ACKNOWLEDGMENTS

We wish to thank Dr. P. Alexander for his help in the preparation of this chapter.

REFERENCES

Akpa, B. S., Mantle, M. D., Sederman, A. J., and Gladden, L. F. J. *Chem. Soc., Chem. Commun.* **2741** (2005).

Altobelli, S. A., Fukushima, E., and Monday, L. A. *J. Rheol.* **41**, 1105 (1997).

Anadon, L. D., Lim, M. H. M., Sederman, A. J., and Gladden, L. F. *Magn. Reson. Imaging* **23**, 291 (2005).

Anderson, M. W., and Klinowski, J. *Chem. Phys. Letts.* **172**, 275 (1990).

Arola, D. F., Barrall, G. A., Powell, R. L., McCarthy, K. L., and McCarthy, M. J. *Chem. Eng. Sci.* **52**, 2049 (1997).

Baba, T., and Ono, Y. *Annu. Rev. NMR Spectroscopy* **38**, 355 (1999).

Balcom, B. J., Carpenter, T. A., and Hall, L. D. *Macromolecules* **25**, 6818 (1992).

Baldwin, C. A., Sederman, A. J., Mantle, M. D., P. Alexander, P., and Gladden, L. F. *J. Colloid Interface Sci.* **181**, 79 (1996).

Bar, N. -K., Bauer, F., Ruthven, D. M., and Balcom, B. *J. Catal.* **208**, 224 (2002).

Bencsik, M., and Ramanathan, C. *Magn. Reson. Imaging* **19**, 379 (2001).

Bertsch, F., Mattner, J., Stehling, M. K., Muller-Lisse, U., Peller, M., Loeffler, R., Weber, J., Messmer, K., Wilmanns, W., Issels, R., and Reiser, M. *Magn. Reson. Imaging* **16**, 393 (1998).

Beuling, E. E., van Dusschoten, D., Lens, P., van den Heuvel, J. C., Van As, H., and Ottengraf, S. P. P. *Biotechnol. Bioeng.* **60**, 283 (1998).

Beyea, S. D., Caprihan, A., Clewett, C. F. M., and Glass, S. J. *Appl. Magn. Reson.* **22**, 175 (2002).

Blok, J. R., Varkevisser, J., and Drinkenburg, A. A. H. *Chem. Eng. Sci.* **38**, 687 (1983).

Boelhouwer, J. G., Piepers, H. W., and Drinkenburg, A. A. H. *Chem. Eng. Sci.* **57**, 4865 (2002).

Bonardet, J. -L., Domeniconi, T., N'Gokoli-Kékélé, P., Spinguel-Huet, M. -A., and Fraissard, J. *Langmuir* **15**, 5836 (1999).

Bows, J. R., Patrick, M. L., Nott, K. P., and Hall, L. D. *Int. J. Food Sci. Technol.* **36**, 243 (2001).

Boyer, C., Duquenne, A. -M., and Wild, G. *Chem. Eng. Sci.* **57**, 3185 (2002).

Britton, M. M., and Callaghan, P. T. *J. Rheol.* **41**, 1365 (1997).

Britton, M. M., Sederman, A. J., Taylor, A. F., Scott, S. K., and Gladden, L. F. J. *Phys. Chem.* (submitted, 2005).

Brunner, E., Haake, M., Kaiser, L., Pines, A., and Reimer, J. A. *J. Magn. Reson.* **138**, 155 (1999).

Buckley, C., Hollingsworth, K. G., Sederman, A. J., Holland, D. J., Johns, M. L., and Gladden, L. F. *J. Magn. Reson.* **161**, 112 (2003).

Butler, L. G., Cory, D. G., Dooley, K. M., Miller, J. B., and Garroway, A. N. *J. Am. Chem. Soc.* **114**, 125 (1992).

Callaghan, P. T., "Principles of Nuclear Magnetic Resonance Microscopy". Clarendon, Oxford (1991).

Caprihan, A., Fukushima, E., Rosato, A. D., and Kos, M. *Rev. Sci. Instrum.* **68**, 4217 (1997).

Cheah, K. Y., Chiaranussati, N., Hollewand, M. P., and Gladden, L. F. *Appl. Catal. A* **115**, 147 (1994).

Chingas, G. C., Miller, J. B., and Garroway, A. N. *J. Magn. Reson.* **66**, 530 (1986).

Chupas, P. J., and Grey, C. P. *J. Catal.* **224**, 69 (2004).

Cormier, R. J., Kilfoil, M. L., and Callaghan, P. T. *Phys. Rev. E* **64** Art. No. 051809 (2001).

Cormier, R. J., and Callaghan, P. T. *J. Chem. Phys.* **116**, 10020 (2002).

Crine, M., Marchot, P., Lekhlif, B., and L'Homme, G. *Chem. Eng. Sci.* **47**, 2263 (1992).

Dankworth, D. C., Kevrekidis, I. G., and Sundaresan, S. *A.I.Ch.E. J.* **36**, 605 (1990).

Dirckx, C. J., Clark, S. A., Hall, L. D., Antalek, B., Tooma, J., Hewitt, J. M., and Kawaoka, K. *A.I.Ch.E. J.* **46**, 6 (2000).

Doran, S. J., Carpenter, T. A., and Hall, L. D. *Rev. Sci. Instrum.* **65**, 2231 (1994).

Duncan, T. M., Winslow, P., and Bell, A. T. *J. Catal.* **93**, 1 (1985).

Dybowski, C., Bansal, N., and Duncan, T. M. *Annu. Rev. Phys. Chem.* **42**, 433 (1991).

Egiebor, N. O., Gray, M. R., and Cyr, N. *Chem. Eng. Commun.* **77**, 125 (1989).
Ehrichs, E. E., Jaeger, H. M., Karczmar, G. S., Knight, J. B., Kuperman, V. Y., and Nagel, S. R. *Science* **276**, 1632 (1995).
Fraissard, F. *Catal. Today* **51**, 481 (1999).
Fukushima, E. *Ann. Rev. Fluid Mech.* **31**, 95 (1999).
Gatenby, J. C., and Gore, J. C. *J. Magn. Reson. A* **110**, 26 (1994).
Gladden, L. F. *Chem. Eng. Sci.* **49**, 3339 (1994).
Gladden, L. F. *Top. Catal.* **24**, 19 (2003).
Gladden, L. F., Alexander, P., and Hollewand, M. P. *A.I.Ch.E. J.* **41**, 894 (1995).
Gladden, L. F., Alexander, P., Britton, M. M., Mantle, M. D., Sederman, A. J., and Yuen, E. H. L. *Magn. Reson. Imaging* **21**, 213 (2003a).
Gladden, L. F., Lim, M. H. M., Mantle, M. D., Sederman, A. J., and Stitt, E. H. *Catal. Today* **79**, 203 (2003b).
Gladden, L. F., Buckley, C., Chow, P. S., Davidson, J. F., Mantle, M. D., and Sederman, A. J. *Curr. Appl. Phys.* **4**, 93 (2004).
Gladden, L.F., Anadon, L.D., Lim, M.H.M., Sederman, A.J., and Stitt, E.H. *Ind. Eng. Chem. Res.* (in press).
Gotz, J., Zick, K., Heinen, C., and Konig, T. *Chem. Eng. Process.* **41**, 611 (2002).
Grosser, K., Carbonell, R. G., and Sundaresan, S. *A.I.Ch.E. J.* **34**, 1850 (1988).
Groten, W. A., Wojciechowski, B. W., and Hunter, B. K. *J. Catal.* **138**, 343 (1992).
Guilfoyle, D. N., Mansfield, P., and Packer, K. J. *J. Magn. Reson.* **97**, 342 (1992).
Haase, A., Frahm, J., Matthaei, D., Hanicke, W., and Merboldt, K. D. *J. Magn. Reson.* **67**, 258 (1986).
Hall, L. D., Amin, M. H. G., Evans, S., Nott, K. P., and Sun, L. *J. Electron. Imaging* **10**, 601 (2001).
Han, S. I., Stapf, S., and Blumich, B. *Phys. Rev. Lett.* **87** Art. No. 144501 (2001a).
Han, S. I., Marseille, O., Gehlen, C., and Blümich, B. *J. Magn. Reson.* **152**, 87 (2001b).
Haw, J. F. *Top. Catal.* **8**, 81 (1999).
Heath, C. A., Belfort, G., Hammer, B. E., Mirer, S. D., and Pimbley, J. M. *A.I.Ch.E. J.* **36**, 547 (1990).
Heine, C., Kupferschlager, K., Stapf, S., and Blümich, B. *J. Magn. Reson.* **154**, 311 (2002).
Heink, W., Kärger, J., and Pfeifer, H. *Chem. Eng. Sci.* **33**, 1019 (1978).
Hennig, J., Nauerth, A., and Friedburg, H. *Magn. Reson. Med.* **3**, 823 (1986).
Hill, K. M., Caprihan, A., and Kakalios, J. *Phys. Rev. Lett.* **78**, 50 (1997).
Holland, D. J., Sederman, A. J., Mantle, M. D., Gladden, L. F., and Middelberg, A. P. J. *J. Chromatogr. A* **1033**, 311 (2004).
Hollewand, M. P., and Gladden, L. F. *J. Catal.* **144**, 254 (1993).
Hollewand, M. P., and Gladden, L. F. *Magn. Reson. Imaging* **12**, 291 (1994).
Holub, R. A., Duduković, M. P., and Ramachandran, P. A. *Chem. Eng. Sci.* **47**, 2343 (1992).
Hong, U., Karger, J., Hunger, B., Feoktistova, N. N., and Zhdanov, S. P. *J. Catal.* **137**, 243 (1992).
Howseman, A. M., Stehling, M. K., Chapman, B., Coxon, R., Turner, R., Ordidge, R. J., Cawley, M. G., Glover, P., Mansfield, P., and Coupland, R. E. *Br. J. Radiol.* **61**, 822 (1988).
Hunger, M., and Weitkamp, J. *Angew. Chem. Int. Ed.* **40**, 2954 (2001).
Jezzard, P., Carpenter, T. A., Hall, L. D., Clayden, N. J., and Jackson, P. *J. Polym. Sci. Pt. B-Polym. Phys.* **30**, 1423 (1992).
Johns, M. L., and Gladden, L. F. *J. Magn. Reson.* **154**, 142 (2002).
Johns, M. L., Sederman, A. J., Bramley, A. S., Alexander, P., and Gladden, L. F. *A.I.Ch.E. J.* **46**, 2151 (2000).
Karger, J., and Freude, D. *Chem. Eng. Technol.* **25**, 769 (2002).
Kauten, R. J., Maneval, J. E., and McCarthy, M. J. *J. Food Sci.* **56**, 799 (1991).
Khitrina, L. Y., Koptyug, I. V., Pakhomov, N. A., Sagdeev, R. Z., and Parmon, V. N. *J. Phys. Chem. B,* **104**, 1966 (2000).

Kimmich, R., ''NMR Tomography, Diffusometry, Relaxometry''. Springer, Berlin Heidelberg (1997).
Kimmich, R., and Hoepfel, D. *J. Magn. Reson.* **72**, 379 (1987).
Koptyug, I. V., Fenelonov, V. B., Khitrina, L. Y., Sagdeev, R. Z., and Parmon, V. N. *J. Phys. Chem. B,* **102**, 3090 (1998).
Koptyug, I. V., Altobelli, S. A., Fukushima, E., Matveev, A. V., and Sagdeev, R. Z., J, *Magn. Reson.* **147**, 36 (2000a).
Koptyug, I. V., Khitrina, L. Y., Arsitov, Y. I., Tokarev, M. M., Iskakov, K. T., Parmon, V. N., and Sagdeev, R. Z. *J. Phys. Chem. B,* **104**, 1695 (2000b).
Koptyug, I. V., Ilyina, L. Y., Matveev, A. V., Sagdeev, R. Z., Parmon, V. N., and Altobelli, S. A. *Catal. Today* **69**, 385 (2001).
Koptyug, I. V., Kulikov, A. V., Lysova, A. A., Kirillov, V. A., Parmon, V. N., and Sagdeev, R. Z. *J. Am. Chem. Soc.* **124**, 9684 (2002).
Koptyug, I. V., Lyosova, A. A., Kulikov, A. V., Krlov, V. A., Parmon, V. N., and Sagdeev, R. Z. *Appl. Catal. A* **267**, 143 (2004).
Kose, K. *Phys. Rev. A* **44**, 2495 (1991a).
Kose, K. *J. Magn. Reson.* **92**, 631 (1991b).
Kose, K. *J. Magn. Reson.* **96**, 596 (1992).
Kose, K. *Phys. Rev. Lett.* **72**, 1467 (1994).
Kuethe, D. O. *Phys. Rev. A* **40**, 4542 (1989).
Kuethe, D. O., and Gao, J. H. *Phys. Rev. E* **51**, 3252 (1995).
Kuethe, D. O., Caprihan, A., Gach, H. M., Lowe, I. J., and Fukushima, E. J. *Appl. Physiol.* **88**, 2279 (2000).
Larachi, F., Iliuta, I., Chen, M., and Grandjean, B. P. A. *Can. J. Chem. Eng.* **77**, 751 (1999).
Laufer, J. *NACA Rep.* **1174**, 1 (1954).
Le Bihan, D., Delannoy, J., and Levin, R. L. *Radiology* **171**, 853 (1989).
Li, T. Q., Seymour, J. D., Powell, R. L., McCarthy, K. L., Ödberg, L., and McCarthy, M. J. *Magn. Reson. Imaging* **12**, 923 (1994).
Lim, M. H. M., Sederman, A. J., Gladden, L. F., and Stitt, E. H. *Chem. Eng. Sci.* **59**, 5403 (2004).
Mair, R. W., Sen, P. N., Hürlimann, M. D., Patz, S., Cory, D. G., and Walsworth, R. L. *J. Magn. Reson.* **156**, 202 (2002).
Mansfield, P., and Grannell, P. K. *J. Phys. C,* **6**, L422 (1973).
Mansfield, P. *J. Phys. C,* **10**, L55 (1977).
Mantle, M. D., and Sederman, A. J. *Prog. Nucl. Magn. Reson. Spectr.* **43**, 3 (2003).
Manz, B., Alexander, P., and Gladden, L. F. *Phys. Fluids,* **11**, 259 (1999a).
Manz, B., Chow, P. S., and Gladden, L. F. *J. Magn. Reson.* **136**, 226 (1999b).
Manz, B., Gladden, L. F., and Warren, P. B. *A.I.C.hE. J.* **45**, 1845 (1999c).
Mariani, N. J., Martínez, O. M., and Barreto, G. F. *Chem. Eng. Sci.* **56**, 5995 (2001).
Martin, N., Viniegra, M., Lima, E., and Espinosa, G. *Ind. Eng. Chem. Res.* **43**, 1206 (2004).
Menzinger, M., Tzalmona, A., Armstrong, R. L., Cross, A., and Lemaire, C. J. *Phys. Chem.* **96**, 4725 (1992).
Metcalfe, G., Graham, L., Zhou, J., and Liffman, K. *Chaos* **9**, 581 (1999).
Mosher, T. J., and Smith, M. B. *Magn. Reson. Med.* **15**, 334 (1990).
Ng, K. M. *A.I.Ch.E. J.* **32**, 115 (1986).
Nott, K. P., and Hall, L. D. *Trends Food Sci. Technol.* **10**, 366 (1999).
Nott, K. P., Paterson-Beedle, M., Macaskie, L. E., and Hall, L. D. *Biotech. Lett.* **23**, 1749 (2001).
Oshio, K., and Feinberg, D. A. *Magn. Reson. Med.* **20**, 344 (1991).
Packer, K. J. *Top. Catal.* **3**, 249 (1996).
Pangrle, B. J., Walsh, E. G., Moore, S. C., and DiBasio, D. *Chem. Eng. Sci.* **47**, 517 (1992).
Parker, W. O. *Comment Inorg. Chem. Part A* **22**, 31 (2000).
Pietraß, T., Seydoux, R., and Pines, A. *J. Magn. Reson.* **133**, 299 (1998).
Pope, J. M., and Yao, S. *Concepts Magn. Reson.* **5**, 281 (1993a).

Pope, J. M., and Yao, S. *Magn. Reson. Imaging,* **11**, 585 (1993b).
Powell, R. L., Maneval, J. E., Seymour, J. D., McCarthy, K. L., and McCarthy, M. J. *J. Rheol.* **38**, 1465 (1994).
Ra'bai, G., Orba'n, M., and Epstein, I. R. *Acc. Chem. Res.* **23**, 258 (1990).
Reinecke, N., and Mewes, D. *Chem. Eng. Sci.* **52**, 2111 (1997).
Rigby, S. P., Cheah, K. Y., and Gladden, L. F. *Appl. Catal. A* **144**, 377 (1996).
Rigby, S. P., and Gladden, L. F. *J. Catal.* **173**, 484 (1998).
Rigby, S. P., and Gladden, L. F. *Chem. Eng. Sci.* **54**, 3503 (1999).
Rigby, S. P., and Daut, S. *Adv. Colloid Interface Sci.* **98**, 87 (2002).
Roe, D. C., Kating, P. M., Krusic, P. J., and Smart, B. E. *Top. Catal.* **5**, 133 (1998).
Sains, M. C., El-Bachir, M. S., Sederman, A. J., and Gladden, L. F. *Magn. Reson. Imaging* **23**, 291 (2005).
Savelsberg, R., Demco, D. E., Blumich, B., and Stapf, S. *Phys. Rev. E.* **56** Art. No. 020301(R) (2002).
Schwarz, H. B., Ernst, H., Ernst, S., Karger, J., Roser, T., Snurr, R. Q., and Weitkamp, J. *Appl. Catal. A* **130**, 227 (1995).
Schwarz, H.B., Ernst, S., Karger, J., Knorr, B., Seiffert, G., Snurr, R.Q., Staudte, B., and Weitkamp, J.J. Catal. 167, 248 (1997).
Scott, S. K. *Acc. Chem. Res.* **20**, 186 (1987).
Sederman, A. J., Johns, M. L., Bramley, A. S., Alexander, P., and Gladden, L. F. *Chem. Eng. Sci.* **52**, 2239 (1997).
Sederman, A. J., Johns, M. L., Alexander, P., and Gladden, L. F. *Chem. Eng. Sci.* **53**, 2117 (1998).
Sederman, A. J., Alexander, P., and Gladden, L. F. *Powder Technol.* **117**, 255 (2001).
Sederman, A. J., and Gladden, L. F. *Magn. Reson. Imaging* **19**, 339 (2001a).
Sederman, A. J., and Gladden, L. F. *Chem. Eng. Sci.* **56**, 2615 (2001b).
Sederman, A. J., Mantle, M. D., and Gladden, L. F. *J. Magn. Reson.* **161**, 15 (2003).
Sederman, A. J., Mantle, M. D., Buckley, C., and Gladden, L. F. *J. Magn. Reson.* **166**, 182 (2004a).
Sederman, A. J., Hollingsworth, K. G., Johns, M. L., and Gladden, L. F., J, *Magn. Reson.* **171**, 118 (2004b).
Seymour, J. D., and Callaghan, P. T. *A.I.Ch.E. J.* **43**, 2096 (1997).
Seeley, J. A., Han, S. I., and Pines, A. *J. Magn. Reson.* **167**, 282 (2004).
Seymour, J. D., Caprihan, A., Altobelli, S. A., and Fukushima, E. *Phys. Rev. Lett.* **84**, 266 (2000).
Sicardi, S., and Hofmann, H. *Chem. Eng. J.* **20**, 251 (1980).
Sie, S. T., Senden, M. M. G., and van Wechem, H. M. H. *Catal. Today,* **8**, 371 (1991).
Silva, A. C., Barbier, E. L., Lowe, I. J., and Koretsky, A. P. *J. Magn. Reson.* **135**, 242 (1998).
Simoneau, C., McCarthy, M. J., Kauten, R. J., and German, J. B. *J. Am. Oil Chem. Soc.* **68**, 481 (1991).
Singer, J. R. *Science* **130**, 1652 (1959).
Stamps, J. P., Ottink, B., Visser, J. M., van Duynhoven, J. P. M., and Hulst, R. *J. Magn. Reson.* **151**, 28 (2001).
Stapf, S., Packer, K. J., Graham, R. G., Thovert, J. F., and Adler, P. M. *Phys. Rev. E* **58**, 6206 (1998).
Stejskal, E. O. *J. Chem. Phys.* **43**, 3597 (1965).
Stejskal, E. O., and Tanner, J. E. *J. Chem. Phys.* **42**, 288 (1965).
Sun, L., and Hall, L. D. *Intl. Commun. Heat Mass Transfer,* **28**, 461 (2001).
Tallerek, U., Albert, K., Bayer, E., and Guiochon, G. *A.I.Ch.E. J.* **42**, 3041 (1996).
Tallerek, U., Vergeldt, F. J., and Van As, H. *J. Phys. Chem. B,* **103**, 7654 (1999).
Tallerek, U., Rapp, E., Van As, H., and Bayer, E. *Angew. Chem. Int. Ed.* **40**, 1684 (2001).
Taylor, G. I. *Proc. Roy. Soc. (London),* **146A**, 501 (1934).
Timonen, J., Alvila, L., Hirva, P., Pakkanen, T. T., Gross, D., and Lehmann, V. *Appl. Catal. A,* **129**, 117 (1995).
Toye, D., Marchot, P., Crine, M., and L'Homme, G. *Meas. Sci. Technol.* **7**, 436 (1996).

Tzalmona, A., Armstrong, R. L., Menzinger, M., Cross, A., and Lemaire, C. *Chem. Phys. Lett.* **174**, 19 (1990).
Tzalmona, A., Armstrong, R. L., Menzinger, M., Cross, A., and Lemaire, C. *Chem. Phys. Lett.* **188**, 457 (1992).
van der Klink, J. J. *Adv. Catal.* **44**, 1 (2000).
Wang, C. -H., and Li, J. *Chem. Eng. Sci.* **53**, 3579 (1998).
Wang, J. A., Chen, L. F., Li, C. L., and Navaro, O. *Stud. Surf. Sci. Catal.* **139**, 53 (2001).
Wang, W., Walton, J. H., and McCarthy, J. L. *J. Food Proc. Eng.* **22**, 11 (1999).
Wood, J., and L F Gladden, L. F. *Appl. Catal. A* **249**, 241 (2003).
Yang, X. Y., Huan, C., Candela, D., Mair, R. W., and Walsworth, R. L. *Phys. Rev. Lett.* **88**, 44301 (2002).
Yuen, E. H. L., Sederman, A. J., and Gladden, L. F. *Appl. Catal. A* **232**, 29 (2002).
Zhang, J. H., Nicholas, J. B., and Haw, J. F. *Angew. Chem. Intl. Ed.* **39**, 3302 (2000).